Experimental Study of SMAW on DSS 2205 and SS 316L for Marine Applications

Dissertation submitted in partial fulfilment of the requirements

for the award of degree

of

Master of Technology in Marine Technology

by

RITESH KUMAR

(Reg.No.2201215006)

Under the Supervision of

Mr. DHIRAJ KUMAR

Department of Marine Engineering

Indian Maritime University, Kolkata Campus

Kolkata – 700088

July 2024

INDIAN MARITIME UNIVERSITY KOLKATA CAMPUS

Department of Marine Engineering

CERTIFICATE

This is to certify that the thesis entitled **" Experimental Study of SMAW on DSS 2205 and SS 316L for Marine Applications"** submitted by **Mr. Ritesh Kumar** (2201215006) of the Department of Marine Engineering, Indian Maritime University (Kolkata Campus), in partial fulfilment of the requirements for the award of the degree of **Master of Technology** in Marine Technology, is a record of bonafide research work carried out under my supervision and guidance.

The content of the dissertation does not form a basis for the award of other degrees to his/her, to the best of my knowledge. The dissertation, in my opinion, is worthy of consideration for the award of the degree of **Master of Technology** in Marine Technology in accordance with the regulation of the Institute.

Mr. Dhiraj Kumar
Supervisor
Indian Maritime University,
Kolkata Campus
Kolkata, West Bengal 700088
India

Dr. Amarish Kumar Shukla
Course Co-ordinator
Indian Maritime University,
Kolkata Campus
Kolkata, West Bengal 700088
India

External Examiner
D.S.P.VIDYASAGAR
FACULTY
IMU, VISAKHAPATNAM
CAMPUS

EVALUATION SHEET

Name of Candidate	Ritesh Kumar
Title of the project	EXPERIMENTAL STUDY OF SMAW ON DSS 2205 AND SS 316L FOR MARINE APPLICATIONS
Specialization	Marine Technology
Date of Examination	30/07/2024

The board approved this dissertation for the exam

External Examiner: (D.S.P.VIDYASAGAR)

Internal Examiner:

COPYRIGHT AND CONSENT FORM

To ensure uniformity of treatment among all contributors, other forms may not be substituted for this form, nor may any wording of the form be changed. This form is intended for original material submitted to the Indian Maritime University, Kolkata Campus (IMU-KC), Kolkata and must accompany any such material in order to be published by the (IMU-KC). Please read the form carefully and keep a copy for your files.

TITLE OF THESIS: Experimental Study of SMAW on DSS 2205 and SS 316L for Marine Applications.

AUTHOR'S NAME and ADDRESS: RITESH KUMAR, 45, VILL+PO-DILIYAN, PS-CHOURI, DIST-BHOJPUR, 802201, BIHAR.

COPY RIGHT TRANSFER

The undersigned hereby assigns to Indian Maritime University, Kolkata Campus (IMU- KC), Kolkata, all rights under copyright that may exist in and to: (a) the above work, including any revised or expanded derivative works submitted to the (IMU-KC), by the undersigned based on the work and (b) any associated written or multimedia components or other enhancements accompanying the work.

CONSENT AND RELEASE

In the event the undersigned makes a presentation based upon the work at a conference hosted or sponsored in whole or in part by the (IMU-KC), the undersigned, in consideration for his/her participation in the conference, hereby grants the (IMU-KC), the unlimited, worldwide, irrevocable permission to use, distribute, publish, license, exhibit, record, digitize, broadcast, reproduce and archive; in any format or medium, Whether now known or hereafter developed:

a) His /her presentation and comments at the conference;

b) Any written materials or multimedia files used in connection with his/her presentation and

c) Any recorded interview him/her (collectively, the “Presentation").

The permission granted includes the transcription and reproduction of the Presentation for inclusion in products sold or distributed by (IMU-KC) and live or recorded broadcast of the Presentation during or after the conference.

In connection with the permission granted in Section 2, the undersigned hereby grants (IMU-KC) the unlimited, worldwide, irrevocable right to use his/her name, picture, likeness, voice and biographical information as part of the advertisement, distribution and sale of products incorporating the Work or Presentation, and releases (IMU-KC) from any claim based on right of privacy or publicity.

The undersigned hereby warrants that the Work and Presentation (collectively, the "Materials") are original and that he/she is the author of the Materials. To the extent the Materials incorporate test passages, figures, data or other material from the works of others, the undersigned has obtained any necessary permissions.

GENERAL TERMS

- The undersigned represents that he/she has the power and authority to make and execute this assignment.
- The undersigned agrees to indemnify and hold harmless the (IMU-KC) from any damage or expense that may arise in the event of a breach of any of the warranties set forth above.
- In the event the above work is not accepted and published by the (IMU-KC) or is withdrawn by the author(s) before acceptance be the (IMU-KC), the foregoing copyright transfer shall become null and void and all materials embodying the work submitted to the (IMU-KC) will be destroyed.
- For jointly authored works, all joint authors should sign, or one of the authors should sign as authorized agent for the others.

Ritesh Kumar

(Reg. no.: 2201215006)

Table of Contents

ACKNOWLEDGEMENTS

I want to take this opportunity to express sincere thanks and appreciation to everyone who helped me finish my project and create this project report. I extend my heartfelt thanks to RAdm. (Dr.) P J Rangachari, (Retd), our esteemed Director of IMU Kolkata Campus, for his unwavering support, encouragement, and provision of library and laboratory facilities for the Preparation of this report.

I seize this opportunity to convey our deepest gratitude and utmost respect to my supervisor and mentor, Mr. Dhiraj Kumar, from the Department of Marine Engineering, for his exceptional guidance, diligent supervision, and constant motivation throughout the project's duration. His invaluable support, immense assistance, wholehearted cooperation, and fruitful discussions throughout the semester are encapsulated within this dissertation.

I want to thank Dr. Amarish Kumar Shukla, our course coordinator, Department of Marine Engineering, IMU Kolkata, for his guidance, assistance, encouragement, and support in getting this project done. His organizational skills and prompt assistance helped us overcome various challenges and ensured the smooth progression of my work.

I would also like to thanks to Mr. Kamala Kanta Das, Welding Shop Technician and Mr. Chinmoy Sarkar, Assisant Professor & OIC Workshop, for helping me to perform the experiment.

Additionally, I would like to thank the Indian Maritime University Kolkata for their support and cooperation in making this research possible by providing the facilities and resources needed. The help they provided was crucial to the accomplishment of the project.

Lastly, I extend my thanks to all those who were involved, directly or indirectly, during the course of this project.

DECLARATION

I certify that

a) The work contained in this thesis is original and has been done by me under the guidance of my supervisor.

b) The work has not been submitted to any other Institute for any degree.

c) I have followed the guidelines provided by the Institute in preparing the thesis.

d) I have conformed to the norms and guidelines given in the Ethical Code of Conduct of the Institute.

e) Whenever I have used materials (data, theoretical analysis, figures, and text) from other sources, I have given due credit to them by citing them in the text of the thesis and giving their details in the references.

Ritesh Kumar

(Reg. no.: 2201215006)

LIST OF FIGURES

LIST OF TABLES

LIST OF ABBREVIATIONS

AISI	American Iron and steel Institute
SS	Stainless Steel
FEM	Finite Element Model
SMAW	Shielded Metal Arc Welding
SEM	Scanning Electron Microscopy
EDS	Energy Dispersive Spectroscope
MIG	Metal Inert Gas
FEA	Finite Element Analysis
ACT	Ansys Customization Toolkit
CAD	Computer-Aided Design
AC	Alternating Current
DCEP	Direct Current Electrode Positive
DCEN	Direct Current Electrode Negative
HAZ	Heat Affected Zone
FZ	Fusion Zone
Nd:YAD	Neodymium-Doped Yttrium Aluminium Garnet
SAW	Submerged Arc Welding
FCAW	Flux-Core Arc Welding
OAW	Oxyacetylene Arc Welding
GTAW	Gas Tungsten Arc Welding
GMAW	Gas Metal Arc Welding
DT	Destructive Techniques
NDT	Non-Destructive Techniques
YS	Yield Strength
UTS	Ultimate Tensile Strength
MS	Mild Steel
DSS	Duplex Stainless Steel
SS	Stainless Steel
WM	Weld Metal
WZ	Weld Zone
HV	Vickers Hardness
HRB	Rockwell Hardness Measured on B Scale
AWS	American Welding Society
DC	Direct Current

LIST OF SYMBOLS

T	Temperature
t	Time
S	Travel speed
V	voltage
I	Current
HI	Heat Input
L	length
q	Heat flux
σ	Stefan-Boltzmann constant
K	Thermal conductivity
ρ	Density

ABSTRACT

Maritime-grade stainless steel, such as Duplex 2205 and 316L, is widely utilized in shipbuilding constructions, cargo tanks, offshore oil rig platforms, and many other maritime sectors. Austenitic and duplex stainless steels are also widely used in a variety of manufacturing industries and other domains. Because of its unique structural combination of ferrite and austenite grains, it has various benefits like high strength, excellent toughness, and resistance to pitting, crevice corrosion, and stress corrosion cracking. In the present study, shielded metal arc welding is used to weld two dissimilar materials DSS 2205 and SS 316L of dimension 60 mm x 60 mm x 2 mm. Two different types of electrodes such as ER2209 and E316L-16 is used to perform the welding, and also the current are varied from 80A to 100A at constant voltages of 24V to investigate the weld quality characteristics. A detailed investigation was conducted into the effects of electrodes and current on the mechanical characteristics and microstructure of welded specimens. Furthermore, the weld deposition has been investigated by weighing the welded sample before and after welding. The results shows that weld deposition initially increases with an increase of welding current from up to 90A, and then it declines from 90 to 100A. Moreover, transient thermal analysis based on FEM is performed by using ANSYS software, and simulated temperature of weld zone is obtained. Infrared thermal imager is used to capture the actual temperature of weld zone. The actual temperature obtained from thermal imager also validates the simulated temperature. Based on micrograph, martensite and austenite formation has been observed in the duplex stainless steel region and ferrite and cementite has been observed in 316L stainless steel region.

This thesis is divided into six chapters. The first chapter provides an overview of steel welding and its applications across various fields, with a focus on the distinguishing features of SMAW welded samples of DSS 2205 and 316L stainless steel. Chapter 2 reviews the literature on various stainless steel processing techniques and the properties of DSS 2205 and 316L stainless steel, including microstructural, mechanical, and thermal analyses using the Ansys software, and their applications. Then, it identifies gaps in the existing literature and sets targets for addressing problem identification. Chapter 3 details the materials and procedures used in this study and discusses the various characterization strategies employed. Chapter 4 presents the results and discussion of SMAW welded DSS 2205 and 316L stainless steel, including an in-depth investigation into how changes in current and electrodes affect the mechanical properties of these materials. Additionally, this chapter uses the Ansys software tool to study temperature distribution and heat flux during the welding of DSS 2205 and 316L stainless steel. Finally,

Chapter 5 provides a comprehensive summary of the study, along with an exploration of the future scope and additional possibilities for ongoing research on SMAW welded DSS 2205 and 316L stainless steel.

Keywords: microstructure, mechanical properties, Duplex 2205, SS316-L, ER2209, electrode material, shielded metal arc welding

CHAPTER 1

INTRODUCTION

Welding is defined as a joining process that produces fusion of materials by heating them to the welding temperature, with or without the application of pressure alone, and with or without the use of filler metal. "In simpler terms, a weld occurs when individual pieces of material are joined together by heating them to a temperature that causes them to soften or melt and fuse into a single unit." Welding is very important in the shipbuilding industry [1]. There are several kinds of welding methods, such as friction welding, laser welding, arc welding, metal inert gas (MIG) welding, Oxy acetylene welding, TIG welding, and Shielded metal arc welding (SMAW), used in shipping industries. But SMAW is a simple and affordable welding technique, it is also known as “stick welding” or manual metal arc welding mostly used in shipping industries [20]. According to the American Welding Society, common applications of welding include construction, pipelines, machinery structures, shipbuilding, job shop fabrication, and repair work [19]. Dissimilar welding allows the joining of materials characterized by good mechanical properties with another material but of lower quality without altering the soundness of the joint, and it must meet the requirements of strength and safety of the structure being joined [2]. Initially, the shipping industry was facing greater difficulty in achieving the required weld strength after welding the two dissimilar base metals. Metal fillers that are appropriate for the materials being joined are chosen to overcome this strength problem [7]. Austenitic stainless steel is divided into the 200 series and the 300 series, which are its two subgroups. Because the 200 series contains more manganese and less nickel, it has a higher yield strength, which limits its use in a wider range of applications. The 300 series, which includes types 304 and 316, are primarily alloyed with nickel, manganese and nitrogen are commonly utilized to minimize the amount of nickel used. The "L" classification in 316L denotes that, in comparison to ordinary 316 steel, this grade of steel has a lower carbon content, which helps to minimize stress corrosion cracking [13]. Austenitic stainless steels remain the most popular grades due to their unique combination of high weldability, strengthening ability, ductility, and toughness even at extra-low temperatures. The good weldability of austenitic stainless steel is affected by the hot cracking that occurs during the welding operation. This defect is referred to the presence of a susceptible chemical composition (low-melting-point constituents such as sulfur) and a high level of restraint or tensile stresses present in the weld [6]. To overcome the problems associated with SS 316L weldment, several metallurgists have

investigated the welding behavior of duplex stainless steel 2205, which has excellent strength relative to SS 316L. "Furthermore, welding duplex stainless steel to other steel types becomes essential when building ship tanks for transporting chemicals because in the 1990s, austenitic steel was the main material used for constructing tanks for chemical cargo carriers." (AISI 316, 316L, and 316LN) [29] and it was not showing the better durability. DSS 2205 stainless steel is not only stronger than conventional marine grade 316L but also has significantly greater strength, because of the more content of nitrogen, nickel, chromium, and molybdenum in this material [5]. DSS 2205 has nearly twice the strength of standard SS 316L. Because austenitic and duplex stainless steels have approximately similar chemical composition and mechanical properties, they are frequently joined in maritime applications to achieve superior durability [8]. Application of DSS 2205 includes pipelines in pipes for offshore oil and gas as well as desalination plants, petrochemical, paper, and pulp industries [3, 26–27]. Most tanks that are constructed today are made of 2205 duplex steel [29]. Because of the several benefits than 316L such as exceptional mechanical properties like high strength, toughness, elasticity modulus, and stress resistance [30].

There are some common welding techniques used in shipbuilding and marine industry [1].

1. Shielded metal arc welding (SMAW)
2. Submerged Arc Welding
3. Gas metal arc welding (GMAW)
4. Gas tungsten arc welding (GTAW)
5. Oxyacetylene Welding (OAW)
6. Flux Core- Flux-cored arc welding (FCAW)
7. High-energy welding processes such as Laser welding

1.1 Shielded metal arc welding (SMAW)

The SMAW method of welding involves creating an electrical circuit with a ground cable that has a clamp to secure it to the workpiece, a welding machine to generate the electricity, and a welding cable with an electrode holder to hold the electrode. By contacting the electrode with the workpiece, causing the electrode to melt, and creating a weld. The consumable electrode provides gas protection to shield the arc and stop the molten filler metal from becoming contaminated by the air, including components to alter the welded metal's mechanical characteristics and stop excessive grain growth, improving the weld metal's mechanical

characteristics and surface cleanliness. Figure 1.1 presents the shielded metal arc welding process.

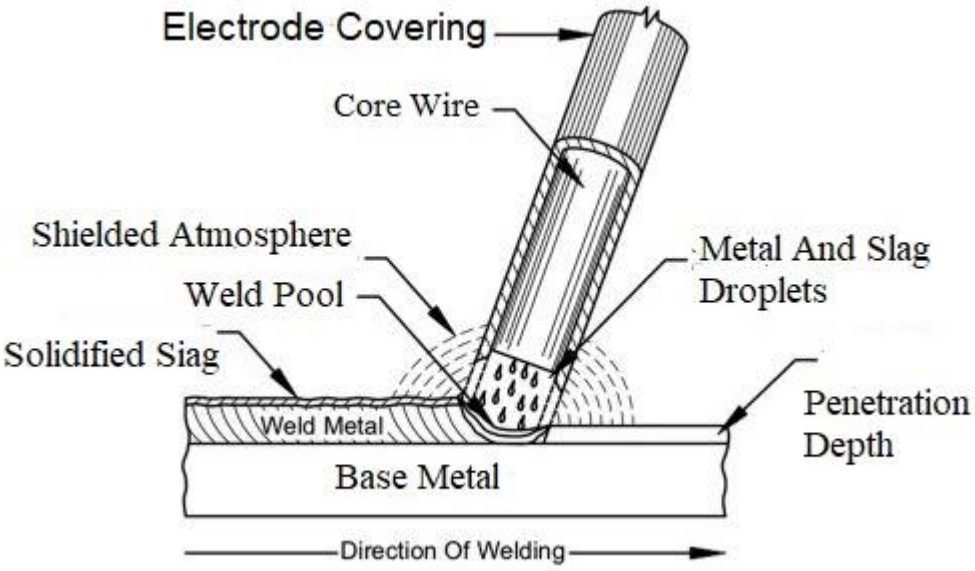

Figure 1.1: Welding of shielded metal arc process (SMAW) [34].

The maintenance and repair sector, the shipping industry, pipelines, offshore platforms, and the building of steel structures, are the industries that use this welding technique. These techniques have the following benefits [1], quick and extremely consistent production of high-quality welds is possible, one machine can combine metals of different kinds and thicknesses, The equipment is inexpensive, easy to use, adaptable, portable, and allows for positional welding, fit for welding in an off-position. The following are drawbacks of this method [1], limited efficiency due to high heat loss.

1.2 Submerged Arc Welding

In submerged arc welding, an electric current flowing between the welding wire and the workpiece forms an arc, which produces the heat needed to fuse the metal. Submerged arc welding flux is a coating of granulated mineral material that covers the workpiece, the arc, and the tip of the welding wire. No visible arc, sparks, splatter, or smoke are present. The end of a bare wire electrode is kept in contact with the work to sustain an arc. A regulated motor powers a set of wheels that feed the melting electrode into the arc. The wire feed speed is automatically adjusted to match the rate of electrode melting. Hence the name "submerged arc," as the arc functions beneath a layer of granular flux. Over the weld pool, some of the flux melts to form a protective layer. As long as the residual flux is clean, dry, and not polluted, it can be retrieved

and utilized again. There is a semi-automatic variant that allows the user to operate a welding gun that holds a tiny amount of flux in a hopper [1]. Figure 1.2 represents the submerged arc welding process.

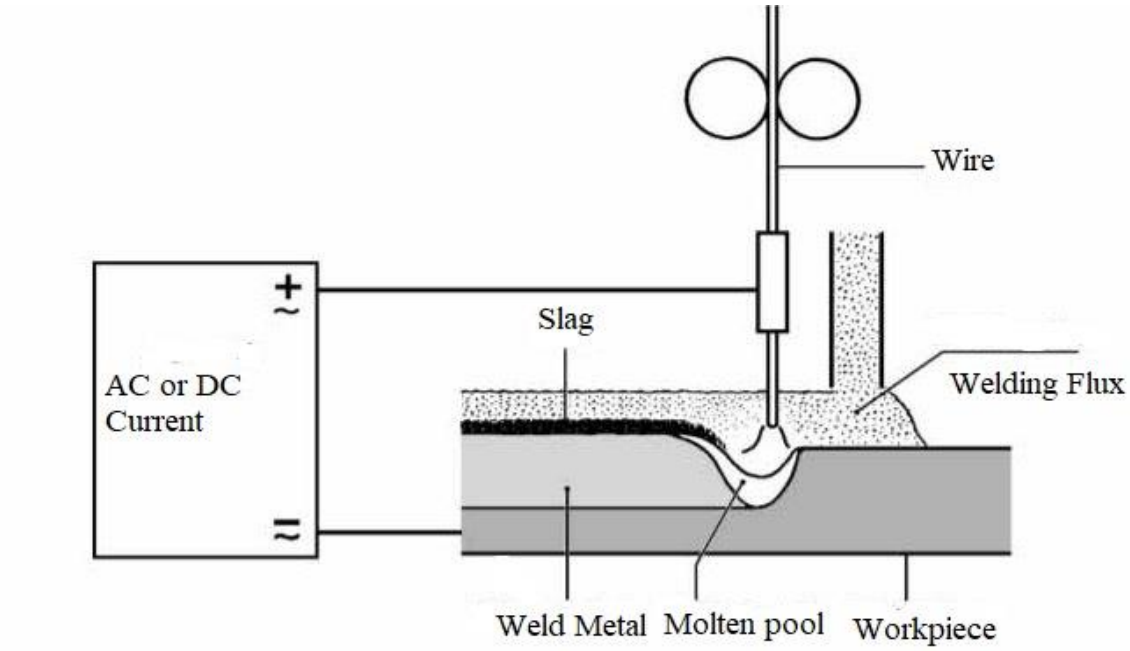

Figure 1.2: Welding of submerged arc process [35].

This type of welding has the following benefits [1], it can produce consistently high-quality welds with a minimum amount of operator skill, the lowest possible level of arc visibility and welding smoke(radiation), Perfect for joining bulky parts together, suitable for low-alloy and carbon steel welding, Comparatively high rates of metal deposition, this type of welding has the following drawbacks[33], welding in a flat or horizontal position only, exercise caution to maintain proper electrode alignment, a strong flux cover is present over the tip and weld pool. thick steel plates are primarily welded using this technique in heavy industries including shipbuilding, the production of large-diameter pipes, and boiler-making [1].

1.3 Gas Metal Arc Welding (GMAW)

Gas metal arc welding (GMAW) is an arc welding technique that heats metals by creating an arc between the work and a filler metal electrode that is continually fed.

The molten weld pool is shielded during the procedure from an external gas supply. Gas metal arc welding (GMAW) is a semi-automatic arc welding method in which shielding gas

and a continuous, consumable wire electrode are fed through a welding gun [1]. Figure 1.3 displays the gas metal arc welding process.

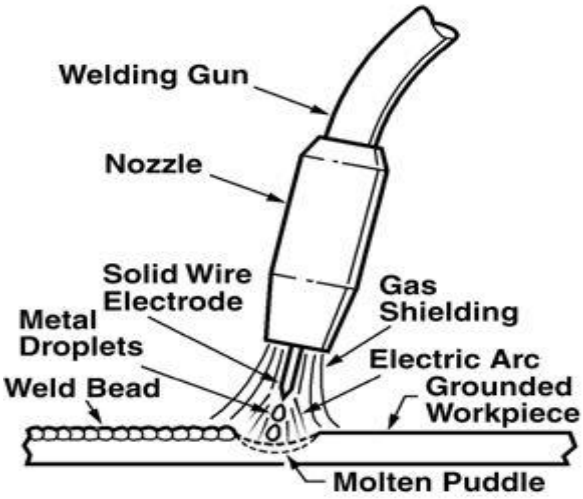

Figure 1.3: Welding of gas metal arc process [36]

1.4 Gas tungsten arc welding (GTAW)

An electric arc is maintained between a non-consumable tungsten electrode and the item to be welded during the gas tungsten arc welding (GTAW), also referred to as the TIG (tungsten inert gas) welding method. A layer of inert gas is pumped through the GTAW torch to protect the molten metal, the tungsten electrode, and the heat-affected zone from airborne pollution. The purpose of the shielding gas is to envelop the weld and keep out the active ingredients in the surrounding air. Argon and helium are inert gases that do not mix or react chemically with other gases. Hydrogen gas may occasionally be supplied to increase travel speeds [1]. Figure 1.4 presents the gas tungsten arc welding process.

The following are GMAW's benefits, welding can be done in any orientation, slag removal is not necessary, and rapid rate of weld metal deposition. The following are the drawbacks of GTAWs , expensive and complicated equipment, equipment setup might be difficult and time-consuming [1].

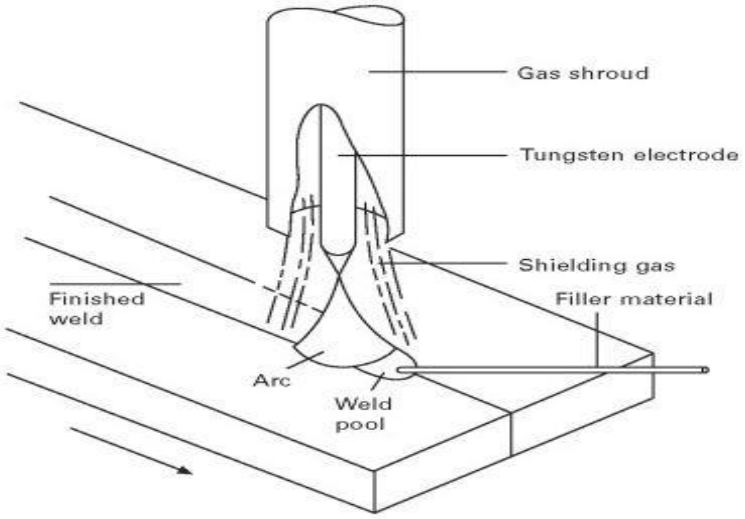

Figure 1.4: Welding of gas tungsten arc process [37]

1.5 Oxyacetylene Welding (OAW)

Oxygen and acetylene gas are combined in the oxyacetylene welding process to create a high-temperature flame. When combined in the proper ratios in a blowpipe or hand torch, a relatively hot flame with a temperature of roughly 3,200 degrees celsius is created. The volume of oxygen to acetylene ratio can be changed to modify the chemical action of the oxyacetylene flame. Steel cylinders are used to hold ethylene and oxygen under pressure [1]. Figure 1.5 displays the oxy-acetylene welding process.

The following are some benefits of oxyacetylene, it's simple to learn compared to most other types of the welding process, the equipment is less expensive. The following are some oxyacetylene drawbacks, oxy-acetylene weld lines are significantly rougher than other types of welds and require additional polishing if neatness is required, oxyacetylene is a manual method that requires the welder to manually regulate the filler rod application and torch movement.

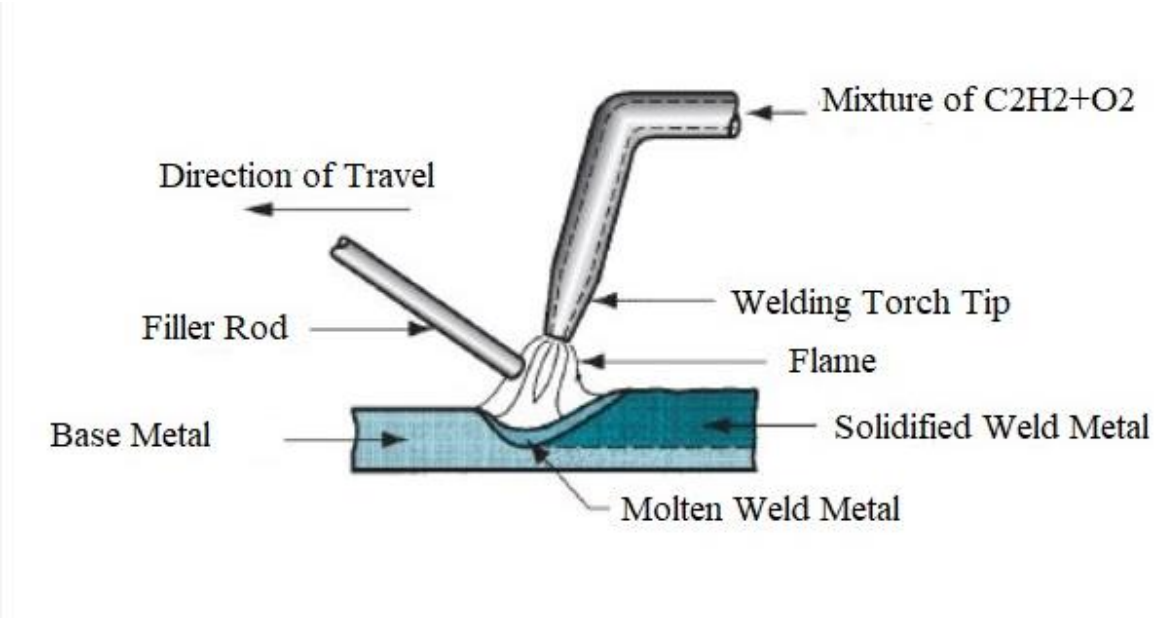

Figure 1.5: Welding of oxy-acetylene [38].

1.6 Flux Core- Flux-cored arc welding (FCAW)

In flux cored arc welding (FCAW), a flux-cored wire is utilized. The components found in the tubular electrode's core offer excellent welding performance in addition to improved weld zone shielding. Gas-shielded FCAW is mostly employed for in-house fabrications, whereas self-shielded FCAW is still utilized for field fabrication. The active gases react with silicon and manganese alloys in the liquid weld metal under the heat of a welding arc, causing these elements to be melt in the solidified weld. In addition to influencing the weld's characteristics, the shielding gas also establishes the penetration pattern and shape. The welding wire and shielding gas combine during the process to create a robust, corrosion-resistant weld. The amount of hydrogen, nitrogen, and oxygen that are still dissolved in the weld metal is likewise impacted by the shielding gas [39]. Figure 1.6 presents the gas-shielded, flux-cored arc welding process.

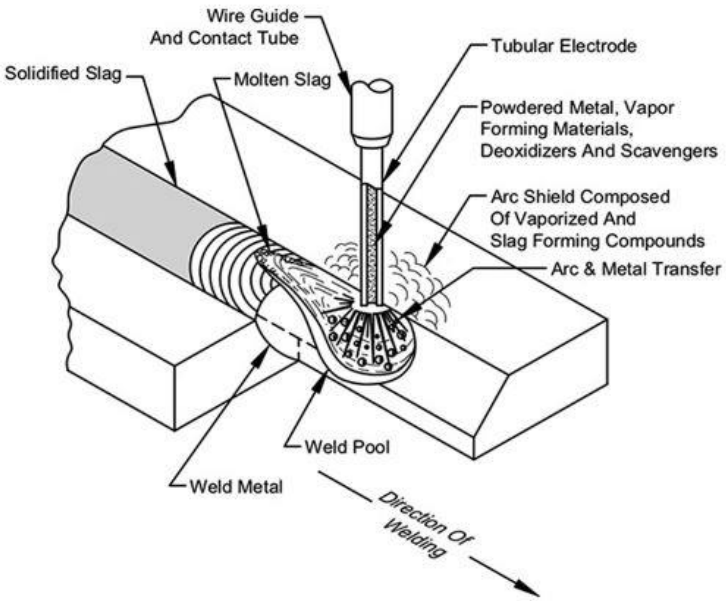

Figure 1.6: Welding of gas-shielded, flux-cored arc process (FCAW-G) [40]

Benefits of Flux-Cored Welding [40], high Welding Speed compared to some other welding processes, flux-cored welding may reach greater deposition rates compared to conventional welding techniques that depend on external shielding gas, the following are some drawbacks of flux-cored welding [40], if the welding parameters are not set correctly, flux-cored welding may result in porosity in the welds. Slag inclusion can occur when slag is lodged in the weld metal as a result of inadequate removal during welding.

1.7 High Energy Beam Welding

Electron and laser beam welding are both high energy beam welding techniques. High power laser applications are desirable because they can quickly weld the thin sheets. Laser welding has several benefits, including smaller flange widths, greater structural strength, and automated processing at rapid speeds. In the past, CO2 lasers were commonly employed in automotive body applications. However, recent improvements in Nd: YAG laser science have made it possible for them to generate beam energies through optical fibre cables with capacities greater than 2kW. This is particularly beneficial for robotic operations that call for leading the laser beam around fixed components. [42]. Figure 1.7 displays the welding of the laser beam process.

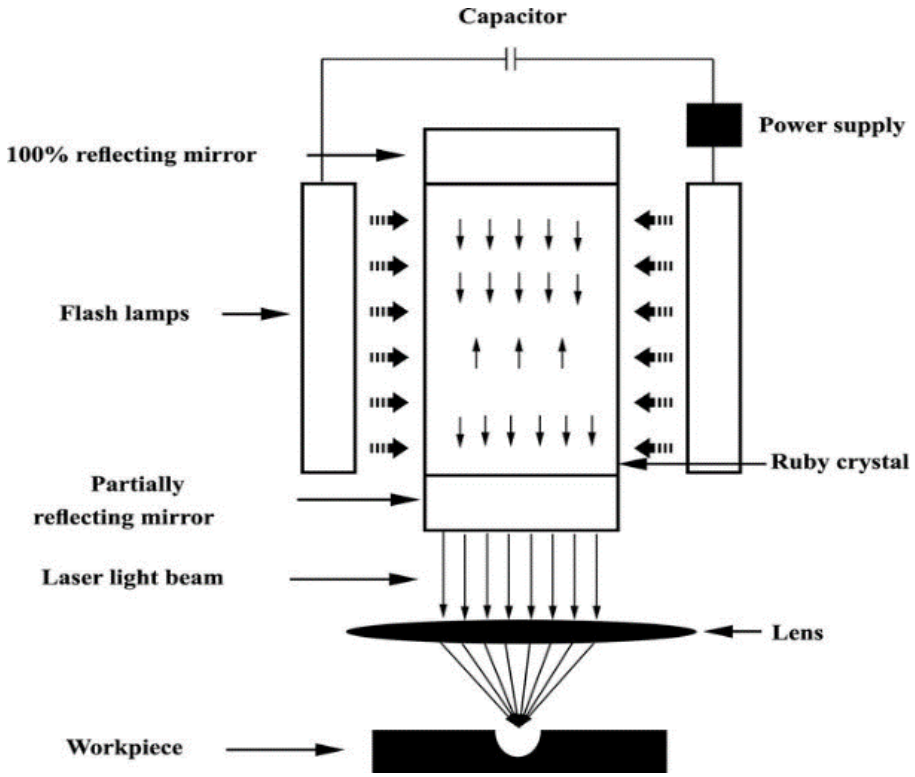

Figure 1.7: Welding of laser beam process [43]

1.8 Shielded Metal Arc Welding Parameter

1.8.1 Arc length

Arc length refers to the distance between the tip of the welding electrode and the surface of the workpiece. This distance is critical because it directly impacts the welding process, including the stability of the arc, the heat input, and the characteristics of the weld bead. Maintaining an appropriate arc length is essential for achieving a stable arc, proper penetration, and a quality weld. Too short an arc length can result in excessive spatter and poor bead shape, while too long an arc length can cause a weak arc, insufficient penetration, and potential defects in the weld [46].

1.8.2 Welding speed

Welding speed refers to the rate at which the welding torch or electrode moves along the seam of the workpiece during the welding process. It is usually measured in inches per minute (ipm) or millimeters per second (mm/s). Welding speed is a critical parameter that influences the

quality, strength, and appearance of the weld. The impacts of welding speed are significant. For penetration, too slow a welding speed can lead to excessive heat input, resulting in deep penetration, which may cause burn-through or warping. Conversely, too fast a speed may result in shallow penetration and weak welds. The speed also affects the shape and size of the weld bead; slower speeds produce wider beads, while faster speeds produce narrower beads. The extent of the Heat Affected Zone (HAZ) is also influenced by welding speed. Slower speeds can enlarge the HAZ, potentially altering the properties of the base material. Moreover, incorrect welding speed can lead to various weld defects such as undercut, porosity, and incomplete fusion. Finding the optimal welding speed is essential for ensuring a strong, high-quality weld [45].

The determined welding speeds are given in Table 1.1 according to the thickness of work piece [45].

Table 1.1: Welding speed based on workpiece thickness.

Workpiece thickness (S)	**Welding speed (Vk), mm/s**	**Welding current (I)**
$S \leq 3$	4.50	d × 40 ampere
$S > 3 \leq 8$	4.00	d×40 ampere
$S > 8$	3.50	d×40 ampere
Work piece thickness (S)	Welding speed(Vk), mm/s	Welding current (I)
$S \leq 3$	4.50	d × 40 ampere
$S > 3 \leq 8$	4.00	d×40 ampere
$S > 8$	3.50	d×40 ampere

1.8.3 Electrode advance angle

The electrode angle in shielded metal arc welding determines the weld quality and characteristics. It affects penetration, weld profile, heat distribution, and slag control. A steeper angle increases penetration and concentrates heat, while a shallower angle reduces penetration and distributes heat evenly. The shape and flow of the weld bead, along with the control of slag movement, are also affected by the angle [44].

The ideal advance angle and tolerance values are given in Table 1.2 which depends on the welding position. The advance angle values are given according to advance direction [44].

Table 1.2: Values of ideal advance angle and tolerances depending on welding position.

Welding position	**Advance angle**	**Tolerance (º)**
Plain weld	80	±5
Cornice (overlap) weld	80	±5
Vertical weld	105	±5
Overhead weld	80	±5

1.8.4 Determining welding current

Welding current is defined as current flowing against the working voltage during the welding process, or when an arc forms. The poles of the welding machine are identified and it is connected to the alternate current. After preparing the cable tips that connect the electrode holders and ground one, the electrode is attached to the holders. When the electrode comes into contact with the work piece, an arc forms, and as a result, a continuous current circle is created. Before applying welding, welders set the welding current [47]. The welding current is not altered while the welding is being applied. However, depending on the welding application, the arc is trimmed or the current can be increased. $I = d \times 40$ is the chosen welding current, which is 40 times the electrode core diameter. This amount is subject to fluctuate by 10% based on the thickness of materials and position.

1.8.5 Selection of electrode diameter

The electrodes utilized in shielded metal arc welding can be classified into main types, joining electrodes and filler welding electrodes. Depending on its intended application, joining electrodes are made specifically to join two metal pieces together, whereas filler welding electrodes are used to add material and fill gaps during the welding process. In contrast, classified based on various factors, including the strength of the weld metal, suitable welding positions, preferred current and polarity, and the type of coating, are the coated electrodes [48]. High strength, ductility, and toughness are desired qualities in an electrode material during welding [49]. Table 1.3 displays the various workpiece thickness and their respective electrode diameter.

Table 1.3: Various work piece thickness and their respective electrodes.

Work piece thickness (s)	Electrode core diameter (d)	Unit
$S \leq 3$	2.5	mm
$3 < S \leq 20$	3.25	mm
$S > 20$	4.00	mm

1.9 Different Types of Currents

There are three distinct types of current used in welding, alternating current (AC), direct-current electrode negative (DCEN), and direct current electrode positive (DCEP) [50].

1.9.1 DCEN (Direct-Current Electrode Negative)

In direct-current electrode negative (DCEN) welding, the workpiece is positively charged while the electrode is negatively charged. This setup causes electrons to travel from the electrode to the metal surface across the arc. Consequently, the metal being welded absorbs about two-thirds of the welding heat, while the electrode absorbs roughly one-third. This distribution leads to a high melting rate of the electrode in DCEN welding [50].

1.9.2 DCEP (Direct-Current Electrode Positive)

In direct-current electrode positive (DCEP) welding, the workpiece is negatively charged while the electrode is positively charged. This causes electrons to travel from the metal surface being welded to the electrode across the arc. Consequently, the electrode absorbs about two-thirds of the welding heat, while the remaining third goes into the metal being welded [50].

1.9.3 AC (Alternating Current)

In an alternating current (AC) setup, the direction of electron flow reverses every 1/120th of a second, causing the electrode and the work piece to alternate between being the anode and the cathode. The anode is the positive side of the arc, while the cathode is the negative side. This rapid switching of current direction evenly distributes the welding heat, with half going to the work piece and half to the electrode. As a result, the weld bead achieves a balance between penetration and build up due to the consistent heating [50].

One of the numerical methods that can be used to accurately solve engineering problems that are either simple or complex is the finite element method. The method was first used in 1956

for aircraft structural problems analysis. Later, within a decade, the potentialities of the method for the solution of various engineering and applied science problems were recognized. The finite element technique has been so well established over the years that today it seems to be one of the best methods for analyzing the efficiency of various practical problems. The basic idea of the finite element method is actually to find the solution to a complicated problem by replacing it with a simpler one [85].

Common FEA applications include mechanical/aerospace/civil/automotive engineering, structural/stress analysis (static/dynamic, linear/nonlinear), fluid flow, heat transfer, electromagnetic fields, soil mechanics, acoustics, biomechanics, etc. The growth of FEA for functional design issues started with the introduction of the electronic computer system. That is, the significance of FEA for design solutions is a collection of algebraic formulas developed to addressed these problems efficiently, by making use of the electronic computer system. Some of the advantages of FEA include, irregular boundaries, loading, materials types, constraints, element size, modification, etc. FEM permits whole layouts to be built, fine-tuned and also optimized prior to design. This effective tool has actually substantially enhanced both the requirement of design styles as well as the method of the style procedure in numerous commercial applications. Using FEM has actually considerably reduced the time needed from idea to the assembly line. The finite element analysis typically includes 3 basic primary steps, pre-processing, solution and post processing. In the pre-processing stage, the designer constructs a design of the component to be assessed in which the geometry is split right into a variety of distinct sub-regions, or "element", linked at distinct points called "nodes". The designer specifies the geometric domain name, the element type to be utilized, the material property of the components (product is specified by its material constants, every aspect needs to be appointed a specific material), the geometric of the components, the element connection (define a specific number of components in a details location, compel the mesh generator to preserve a certain component dimension), boundary conditions and loading. The dataset prepared by the pre-processor is utilized as input in the solution stage which constructs and addresses a system of nonlinear or direct algebraic equations. The solution is derived by collecting all defined information such as load application (that include pressure, moment, force, rotations) after specifying the entire problem. With the postprocessor software you can visualize the outcomes, for instance, the plot form of the geometry deformation or stress values or anxieties using advanced regimens made use of for arranging, printing, and also outlining results from a finite element solution. A variety of prominent finite element analysis brand are

currently readily available. A few of the preferred bundles are STAAD-PRO, GT-STRUDEL, ABAQUS, NASTRAN, NISA as well as ANSYS [86].

Ansys is one from many of the commonly utilized products in the market for FEA. Ansys, Inc. develops a wide range of computer-aided engineering CAD products, however best recognized for Ansys mechanical/multi physics. FEA tool Ansys is a self-contained analyzing tool, which includes pre-processing, solver, and post-processing divisions. It can be pointed out that Ansys is capable of user programming. The tool command language contains ten hundred command, which can be used to program or modify mesh, geometry, boundary conditions, and many other futures. Therefore, interactive and batch modes are used when dealing with FEA in ansys. The batch mode needs commands to be inputted for the analysis to run and is used mainly by those who are familiar with the Ansys command language. Consequently, the interactive mode refers to visualization, where a graphical interface is used to input data, select options, etc [87].

CHAPTER 2

LITERATURE REVIEW

2.1 Literature Review of Different Researchers

Numerous investigations on materials, microstructural and mechanical characteristics, and thermal analysis using SMAW welding processes, among other techniques, have been carried out. Diverse techniques including distinct welding parameters have been examined.

Jian Luo et al. [51] carried out a study on the submerged arc double-sided single-pass welding of DSS 2205. This study explores the microstructural and mechanical changes in 2205 duplex stainless steel (DSS) weldments. It is observed that the heat input from the subsequent weld pass greatly affects the microstructure of the preceding weld pass, especially in the fusion zone. Notably, there was an increase in the amount of sigma (σ) phase in the fusion zone of the primary weld side, transitioning from a scattered to a continuous distribution. This phase transformation was accompanied by re-melting in the center of the weld transition zone, which reduced the σ phase content. In terms of micro hardness, the fusion zone of the primary weld side exhibited higher values compared to the secondary side, with the weld transition zone displaying the lowest micro hardness. The mechanical properties of the welded joints also varied significantly. The average tensile strength was measured at 795 MPa with fractures occurring predominantly in the fusion zone, where σ phase particles were present on the tensile fracture surfaces. The study concludes that the subsequent welding pass acts as a heat treatment on the initial pass, promoting the formation of the σ phase in the fusion zone, which significantly affects the ductility, toughness, and hardness of the welded joint. This highlights the importance of precise heat input control in the DSSP-SAW of 2205 DSS to manage σ phase formation and optimize joint properties. The findings offer valuable insights into the microstructural evolution and mechanical behavior of these joints, suggesting that further research could focus on optimizing welding parameters to minimize detrimental phase formation while maintaining overall weld quality.

Mohammed et al. [52] reported a study on the effect of the welding process variables on the mechanical, pitting, and microstructure behaviour of 2205 duplex stainless steel weldment. Duplex stainless steels (DSS) is chosen as work material, because of extensive application in various industries, including petrochemical, oil and gas, and paper and pulp. This study aims

to compare the effects of conventional gas tungsten arc welding (GTAW) and activated GTAW (A-GTAW) processes on 2205 DSS. DSS plates of 6 mm thickness were welded using both GTAW and A-GTAW with SiO2 flux. This research involves a thorough examination of the welds' macrostructure, microstructure, hardness, and tensile properties. Microstructural analysis is conducted using optical microscopy and image analysis software. Mechanical properties were assessed through hardness, tensile test. Key findings include a significant difference in weld penetration between the two methods; A-GTAW achieved 52% deeper penetration (5.4mm) compared to GTAW (2.8mm) in a single pass, along with an 11% narrower weld bead width. The microstructure of the base metal shows fine grains of ferrite and austenite. The GTAW weld zone contained grain boundary austenite, Widmanstätten austenite, and intergranular austenite, whereas the A-GTAW weld zone shows grain boundary and Widmanstätten austenite. Notably, the A-GTAW weld zone exhibited a lower ferrite content (43%) compared to the GTAW weld zone (71%). In terms of mechanical properties, a slight increase in hardness is observed in the weld zones relative to the base metal. While GTAW welds demonstrated higher yield strength and tensile strength than A-GTAW, both welding methods met the minimum tensile strength requirements. Regarding strength, A-GTAW welds shows superior performance compared to GTAW and the base metal attributed to the reduced galvanic interaction between austenite and ferrite phases. The study concludes that the A-GTAW process offers advantages over conventional GTAW, particularly for welding 2205 DSS plates. A-GTAW not only achieves deeper penetration but also produces welds with comparable mechanical properties. These benefits are primarily due to the microstructural changes induced by the activated flux and the arc constriction effect inherent to the A-GTAW process.

R. selva et al. [53] studied the parametric effects of plasma arc welding of 2205 duplex stainless steel. Duplex stainless steels contains both ferrite and austenite phases, giving them a unique combination of high-strength. These properties make them particularly well-suited for demanding applications such as pressure vessels and heat exchangers. However, welding of duplex steels presents challenges, primarily due to potential microstructural changes and the precipitation of secondary phases that can occur during the process. Plasma Arc Welding (PAW) is a fusion welding technique known for its deep penetration capabilities and controlled heat input, making it a promising method for welding duplex steels. Previous studies have demonstrated the suitability of PAW for this application. The objectives of the study is to optimize PAW parameters such as current, welding speed, and arc length to analyse their

effects on weld bead geometry and microstructure. To optimize the welding process parameters, the study employs a combination of advanced techniques, including the Taguchi method, Analysis of Variance (ANOVA), Back Propagation Neural Network (BPNN), and Genetic Algorithm (GA). These optimization methods have been previously utilized in literature for refining welding parameters, and their use in this study aims to improve the quality and properties of the welded joints. The review of existing literature provides an overview of the microstructural changes that occur during the welding of duplex steels, including the formation of ferrite, austenite, and secondary phases. It also highlights how these microstructural changes can affect the mechanical properties of the weld. It emphasizes the need to correlate welding process parameters with weld bead geometry and microstructure to achieve optimal results.

N.A. McPherson et al. [54] investigated the microstructural changes and mechanical properties of a welded duplex stainless steel. The objective of this study is to evaluate the microstructure and properties of duplex stainless steel (grade 2205) welds produced using different welding processes commonly employed in shipbuilding. This study also aim to compare the effects of high (250-350°C) and low (<150°C) interpass temperatures on these welds. Several welding processes were utilized, including Submerged Arc Welding (SAW), Manual Metal Arc Welding (MMAW), and Flux Cored Arc Welding (FCAW). ER 2209 electrodes were used as a filler material for all welds. The evaluation of the welds' properties involved mechanical testing, chemical analysis, optical microscopy, transmission electron microscopy (TEM), and corrosion testing. It is found out that controlling the interpass temperature to below 150°C increased the average ferrite content in both the heat-affected zone (HAZ) and the weld metal, approaching 50%. However, this lower interpass temperature did not significantly affect the mechanical properties of the welds. No intermetallic or carbide phases were found in the weld metal across any of the welding processes. Although, some carbide phases were observed in the HAZ. Lower interpass temperatures results in finer microstructures within the weld metal. No secondary austenite was observed in any weld metal specimens. The HAZ exhibited high dislocation density, deformation bands, twins, and stacking faults. The weld metal elongation occasionally approached the minimum specification of 25%. The impact toughness at -60°C was found to be lower for SAW compared to the other processes. It was also noted that the toughness of the HAZ decreased as the ferrite content increased from 34% to 70%. The study suggest that strain-affected regions in the HAZ might potentially enhance corrosion resistance. The author reported that higher heat inputs did not negatively impact the properties of the

welds, challenging traditional concerns. It was found that controlling the interpass temperature had a more significant influence on the microstructure than on the mechanical properties. The results suggest the potential for using higher heat input welding in applications involving duplex stainless steel, provided that the HAZ properties are not adversely affected. The research has practical implications for optimizing welding processes in shipbuilding and similar applications using duplex stainless steels.

Xiaodong Hu et al. [55] carried out a study on the microstructure formation and its effect on mechanical properties for duplex stainless steel 2205 plasma arc welded joint. This study examines the microstructure development and mechanical properties of plasma arc welded (PAW) joints in SAF2205 duplex stainless steel (DSS). However, maintaining a phase balance of approximately 50% ferrite and 50% austenite during welding is challenging due to the rapid thermal cycles involved. Various welding methods have been investigated to control this phase balance, with mixed results. For instance, friction stir welding can refine grains but often increases ferrite content and precipitates brittle phases. Tungsten inert gas welding typically results in excess ferrite in the heat-affected zone, while laser beam welding can cause excess ferrite due to nitrogen loss. Submerged arc welding, though capable of achieving phase balance, may also lead to the formation of brittle phases. Plasma arc welding (PAW) offers several advantages for DSS, including high energy density, low heat input, and strong penetration, which can produce narrow, high-quality welds with a minimal heat-affected zone. The addition of filler wire in PAW may also help achieve balanced phase ratios in DSS joints. The cooling rate and time spent at temperatures between 800-1200°C significantly influence the final phase ratios. Despite attempts to control the phase balance, issues such as grain coarsening and distortion can still occur in DSS welds. The weld metal often exhibits higher hardness compared to the base metal, while tensile strength may be comparable or slightly reduced. Impact toughness generally decreases in the weld zone.

Jian Luoa et al. [56] reported a study on the microstructure of 2205 duplex stainless steel joint in submerged arc welding by post-weld heat treatment. However, the welding process can lead to the precipitation of problematic second phases that adversely affect the performance of welded joints. Post-weld heat treatment (PWHT) is occasionally employed to address these issues, but the effects of PWHT on the microstructure of 2205 DSS need further exploration. In this study, submerged arc welding (SAW) was used to join plates of 2205 DSS. Some of the welded joints were subsequently subjected to PWHT at 650°C for 0.5 hours. The microstructure of the welded joints was analyzed using optical microscopy, X-ray diffraction

(XRD), and microhardness testing to assess the impact of PWHT. In the absence of PWHT, the σ phase precipitated in the heat-affected zone (HAZ) and along the fusion edge. Additionally, small amounts of χ and γ2 phases were observed in the weld center. This microstructural configuration resulted in microhardness peaks in both the HAZ and the weld center. PWHT is found to be effective to improve the microstructure in the HAZ by dissolving the σ phase. Nevertheless, it also promotes the segregation of phases in the weld center, leading to changes in phase composition and associated microhardness variations. This study also highlights that, although, PWHT offers some benefits, but it has also drawbacks concerning phase segregation. The authors propose a mechanism to explain the phase transformations occurring during welding and PWHT, providing valuable insights for optimizing welding procedures and heat treatments for 2205 DSS joints.

N.A. McPherson et al [57] reported a comparative study on performance of submerged arc welding and the laser welding of stainless steel. This paper explores submerged arc welding (SAW) and laser welding of austenitic and duplex stainless steels. The authors aim to reassess welding practices, particularly focusing on high dilution SAW, and compare these methods to emerging laser welding techniques. The author performed experiments using high dilution SAW on 316LN austenitic and 2205 duplex stainless steels with various weld preparations. It is found out that single-pass, single-sided welds with square edge preparations yielded acceptable properties, despite high heat inputs. The mechanical properties, corrosion resistance, and microstructure were evaluated across different weld configurations. Transmission electron microscopy (TEM) provided detailed examination of the weld microstructures. In 316LN welds, small amounts of chi (χ) phase and occasional sigma (σ) phase were observed, but these did not significantly affect the properties. In duplex 2205 welds, there was minimal precipitation in the weld metal. This study also evaluated laser welding on thinner plates (6-7.5 mm) of both steel types. The laser welds exhibited higher hardness compared to SAW, and their microstructures differed, with some areas in 316LN appearing fully austenitic. TEM analysis revealed higher dislocation densities and some unexpected precipitates, including χ phase and Cr2N, in the laser welds. The findings indicate that high dilution SAW is viable for both 316LN and 2205 stainless steels. Laser welding showed potential advantages, especially in reducing distortion, but raised concerns regarding ferrite content and precipitation. The authors propose hybrid laser-MIG welding as a potential future direction, combining the benefits of laser welding with improved fit-up tolerance. Overall, the study demonstrates that high dilution SAW can be successfully applied to 316LN and 2205

stainless steels, contrary to traditional beliefs. While laser welding offers promising benefits, further investigation is needed, particularly regarding its microstructural effects and industrial applicability. This paper contributes to the field by challenging established welding practices for stainless steels and providing a comparative analysis of SAW and laser welding techniques. It underscores the importance of detailed microstructural analysis in understanding weld properties and suggests areas for future research in stainless steel welding.

Aswin et al. [58] investigated the microstructural, mechanical, and thermal analysis of SS316L weldment for marine engineering applications. This paper presents a comprehensive study on the microstructural, mechanical, and thermal analysis of SS316L weldments produced using shielded metal arc welding (SMAW) for marine engineering applications. SS316L austenitic stainless steel is chosen as the base material for its excellent corrosion resistance and mechanical properties, which are particularly valuable in marine and shipbuilding industries. Two types of electrodes, E316L-16 and E308L-16, were employed in the welding process. The SMAW technique was utilized with varying welding currents of 70A, 80A, and 90A, all at a constant voltage of 24V, and single pass butt joint welding was performed to minimize heat input and distortion. The microstructural analysis was conducted using optical microscopy and scanning electron microscopy (SEM), revealing that the fusion zone exhibited a microstructure consisting of ferrite and austenite. Finer grain structures were observed near the weld zone, while coarser grains were found in the heat-affected zone (HAZ). Mechanical properties were evaluated through microhardness testing and tensile testing, showing that microhardness increased in the fusion zone compared to the base material, with the highest hardness (223 HV) observed in the sample welded with the E316L-16 electrode at 80A current. The tensile strength of the welded joints varied from 190-262 N/mm², which was lower than the base material's 565 N/mm², primarily due to HAZ softening. This study also examined the effect of increasing welding current, which led to higher welding speeds and reduced heat input. It was noted that the width of the welded zone increased with the current from 70A to 80A but decreased at 90A, with optimal mechanical properties achieved at 80A current for both electrode types. Thermal analysis and temperature distribution were simulated using ANSYS software, showing temperature distribution across the weld with maximum temperatures ranging from 566°C to 2121°C depending on welding parameters. The simulations indicated that shorter welding times resulted in lower temperatures, consistent with reduced heat input. The findings demonstrate the significant influence of welding parameters and electrode choice on the microstructure, mechanical properties, and thermal behavior of SS316L weldments. This study

provides valuable insights for optimizing SMAW processes for marine engineering applications using SS316L steel, highlighting the importance of careful selection of welding parameters and materials to achieve desired properties in the weldments.

Santina et al. [59] conducted a research work on simulation of properties of dissimilar welded joints of duplex 2205 and austenitic 316L stainless steel, and investigated the mechanical properties of dissimilar welded joints between duplex 2205 stainless steel and austenitic 316L stainless steel, by employing both experimental testing and computer simulation. This duplex steel also offers superior durability compared to austenitic steels. In the welding process, four types of butt joints were prepared using AVESTA P5 austenitic filler wire, including two-pass and multi-pass welds with varying heat inputs. Charpy impact test and toughness tests is conducted and also examine the microstructure. A finite element model of the welded joint was created based on metallographic observations and mechanical test results, analysing stress and strain distributions under axial loading conditions. The key findings indicated that a multi-pass weld, exhibited the highest average fracture energy, while the heat-affected zone (HAZ) on the 316L side shows the highest toughness and the weld fusion zone displayed the lowest toughness. Stress concentrations were observed in the HAZ of the 2205 steel side in the simulations, with the precipitation of M23C6 carbides potentially contributing to fractures in this region. The study also concluded that there is a negative correlation between heat input during welding and joint toughness, identifying the 2205 HAZ as the most probable fracture location. The authors observed that computer simulation results showed good agreement with experimental observations, emphasizing the importance of using material parameters obtained from real specimens to create reliable simulation models for predicting joint properties. This study provides valuable insights into the mechanical behavior of dissimilar welded joints between duplex and austenitic stainless steels, which is relevant for various industrial applications requiring high strength.

Labanowski et al. [60] performed a research work on stress corrosion cracking at welded joints between duplex and austenitic stainless steels and investigated that the stress corrosion cracking behavior of dissimilar welded joints between duplex and austenitic stainless steel combination increasingly common in chemical tanker construction. Duplex steels are becoming more prevalent due to their strength but austenitic steels are still frequently used. The authors highlight the use of submerged arc welding (SAW) for thick plate welding in shipbuilding, citing its high efficiency. However, concerns arise with the high heat inputs associated with SAW, as they can lead to excessive ferrite content in duplex steels and reduced

ferrite in austenitic steels, potentially compromising corrosion resistance. In the study, 15 mm thick plates of 2205 duplex steel and 316L austenitic steel were welded using Cr23Ni9Mo3 wire and flux. Three joint designs—Y, 2Y, and I groove preparations—were tested, with welding parameters including linear energies ranging from 1.14-3.2 kJ/mm. Various tests, including microstructure analysis, ferrite content measurement, mechanical testing, and slow strain rate testing (SSRT) for stress corrosion in boiling MgCl2 and neutral glycerine, were conducted. The weld metal exhibited dendritic austenite within a ferritic matrix, and narrow heat-affected zones (HAZ) were observed on both sides of the steel. The ferrite content in the duplex HAZ increased to 62-69% compared to the base metal, while no grain growth or intercrystalline fractures were observed in the austenitic HAZ. All welded joints failed in the 316L base metal during tensile tests but passed bend tests with no cracking up to a 120° bend angle. In neutral glycerine, specimens failed on the 316L side, whereas in MgCl2, failures occurred in the duplex HAZ. In this study it has been also noted that a significant reduction in ductility and strength in MgCl2 compared to glycerine, with cracking along ferrite/austenite boundaries or through ferrite grains occurred. The different welding heat inputs did not significantly affect the stress corrosion behavior, but the HAZ of the duplex steel side exhibited reduced corrosion resistance in the MgCl2 environment. The authors conclude that the microstructure of dissimilar austenitic-duplex joints significantly affects stress corrosion behavior, identifying the duplex steel HAZ as the weak point. They also note that the range of welding heat inputs tested (1.15-3.2 kJ/mm) did not materially impact corrosion resistance. This study provides valuable insights into the stress corrosion behavior of dissimilar austenitic-duplex welded joints, particularly relevant for chemical tanker construction and other applications using these materials. The findings emphasize the importance of controlling the HAZ microstructure in duplex steels to maintain corrosion resistance in aggressive environments.

Jagesvar et al. [61] performed a comparative study on the effect of electrode on microstructure and mechanical properties of dissimilar welds of 2205 austeno-ferritic and 316L austenitic stainless steel. The study investigates that the weldability, microstructure, and mechanical properties of dissimilar welds between 2205 duplex stainless steel (DSS) and 316L austenitic stainless steel (ASS) using shielded metal arc welding (SMAW) with two different electrodes - E2209 (duplex) and E309L (austenitic). A single pass SMAW process was employed in direct current electrode positive (DCEP) mode. The microstructural analysis revealed that the E2209 weld solidified in a fully ferritic mode, featuring allotrophicmorphs, Widmanstätten austenite,

and intragranular austenite, while the E309L weld solidified in a ferrite-austenite mode with skeletal and lathy ferrite in an austenitic matrix. The ferrite content was measured to be 35-38% in the E2209 weld and 18-22% in the E309L weld. In terms of hardness, the E2209 weld exhibited a higher value of 237.5 HV compared to 198.8 HV for the E309L weld. Tensile testing indicated that the E2209 weld had a tensile strength of 557 MPa, whereas the E309L weld had a tensile strength of 532 MPa, with both welds fracturing in the 316L base metal, demonstrating adequate weld strength. The impact toughness was approximately 72 J for the E2209 weld and around 60 J for the E309L weld. This study concluded that the E2209 electrode produced welds with superior overall properties compared to the E309L electrode for this dissimilar joint combination. The enhanced properties of the E2209 welds were attributed to the higher chromium and molybdenum content, the presence of nitrogen, a fully ferritic solidification mode, and higher ferrite content. This study provides valuable insights into electrode selection for dissimilar welding of duplex and austenitic stainless steels, underscoring the benefits of using a duplex electrode (E2209) over an austenitic electrode (E309L) in terms of microstructure and mechanical properties.

Shaogang et al. [62] performed a research on the characterization of microstructure, mechanical properties, and corrosion resistance of dissimilar welded joint between 2205 duplex stainless steel and 16MnR, and investigated that the duplex stainless steels (DSS) are known for their excellent mechanical properties and corrosion resistance, primarily due to their balanced austenite-ferrite microstructure. However, joining DSS with low alloy steels presents significant challenges, stemming from differences in composition and thermal properties between the two materials. Despite the importance of understanding these challenges, there is limited research on the microstructure-property relationships for dissimilar welds involving DSS and low alloy high-strength steels. This study explores the welding of 2205 DSS and 16MnR low alloy steel using gas tungsten arc welding (GTAW) and shielded metal arc welding (SMAW), employing ER2209 filler wire for GTAW and E2209 electrode for SMAW. The investigation includes detailed microstructural analysis using optical microscopy, scanning electron microscopy (SEM), transmission electron microscopy (TEM), and X-ray diffraction (XRD), as well as mechanical property assessments through tensile testing, impact testing, and hardness measurements. Corrosion resistance was evaluated using electrochemical testing in a 3.5% NaCl solution. The findings reveal the formation of an unmixed zone and a decarburized layer at the 16MnR-weld metal interface, with the weld metal primarily consisting of austenite and acicular ferrite. No detrimental phases such as sigma or M23C6 carbides were detected.

The tensile strength of the welds was found to be comparable to the 16MnR base metal, while impact toughness varied, with the SMAW joint showing slightly higher toughness due to greater heat input. Hardness peaked at the weld interface due to carbon migration, and corrosion resistance was highest in the DSS base metal, followed by the GTAW and SMAW joints. The study concludes that while both GTAW and SMAW produced acceptable joints, GTAW was more suitable for these dissimilar metal welds, offering better corrosion resistance and mechanical performance. This comprehensive analysis provides valuable insights for selecting welding procedures for DSS-low alloy steel joints in practical applications.

Moteshakker et al. [64], conducted research to explore the characteristics hardness and tensile properties of dissimilar welds joints between SAF 2205 and AISI 316L, and investigated that stainless steels are widely utilized in various industries due to their excellent mechanical properties and corrosion resistance. Welding, a critical fabrication technique, is commonly used for joining stainless steels. Among the different types of stainless steels, austenitic stainless steels like 316L are renowned for their outstanding corrosion resistance, ductility, toughness, and weldability. Another important class, duplex stainless steels such as SAF 2205, features a two-phase microstructure consisting of nearly equal parts ferrite and austenite, which imparts higher strength and enhanced corrosion resistance compared to austenitic grades. In many industrial applications, including the oil & gas and petrochemical sectors, dissimilar metal welding between various stainless steels is often necessary. The selection of appropriate filler metals is crucial for ensuring sound weld joints. In this study, the gas tungsten arc welding (GTAW) process was employed, utilizing SAF 2205 duplex stainless steel and AISI 316L austenitic stainless steel plates as base metals. The filler metals used were AWS ER 347, AWS ER 316L, and AWS ER 309L welding wires. Pure argon was used as the shielding gas during the GTAW process. The microstructure of the welds was examined using optical microscopy and scanning electron microscopy/energy dispersive spectroscopy (SEM/EDS). Additionally, the mechanical properties were evaluated through microhardness testing and tensile testing. The investigation revealed that the weld metals contained skeletal ferrite (dark regions) within an austenite matrix (light regions). Ferrite was found to be enriched in chromium (Cr) and molybdenum (Mo), while austenite was enriched in nickel (Ni). Notably, the ER 309L weld metal exhibited a higher ferrite content due to its higher chromium content. Furthermore, the presence of sigma phase and Nb-rich precipitates was observed in the ER 347 weld metal. The hardness measurements indicated that the weld metals had hardness values between those of the duplex and austenitic base metals. The ER 309L weld metal displayed the highest hardness,

attributed to its higher ferrite content. In terms of mechanical performance, the ER 309L weld metal demonstrated the highest strength and ductility. In contrast, the ER 347 weld metal showed the lowest ductility, which was associated with the presence of brittle precipitates. Fracture analysis revealed that failure occurred in the weld metal for ER 347, while for the other filler metals, fracture occurred in the 316L base metal. Fractographic analysis showed that the ER 347 exhibited a mixed ductile-brittle fracture with cleavage regions, whereas the ER 316L and ER 309L weld metals exhibited fully ductile fractures characterized by dimpled features. In conclusion, the ER 309L filler metal provided the best combination of strength, ductility, and hardness for the dissimilar stainless steel joint. The presence of brittle sigma phase and Nb-rich precipitates in the ER 347 weld metal contributed to reduced ductility and premature failure. The higher ferrite content in the ER 309L weld metal played a significant role in enhancing the strength and hardness of the welds. This paper provides a comprehensive analysis of the microstructure-property relationships in dissimilar stainless steel welds, highlighting the impact of filler metal composition on weld metal microstructure and mechanical performance.

A.vinoth et al. [65] conducted a study on the structure-property relationship of the dissimilar weld between austenitic stainless steel 316L and duplex stainless steel 2205. This study demonstrates the Austenitic stainless steels like 316L have been widely used in marine applications due to their strength. However, they can become susceptible to SCC in severe chloride environments. Duplex stainless steels (DSS), such as 2205, are emerging as alternatives because of their higher yield strength and excellent SCC resistance. Despite their advantages, DSS can be more challenging to weld than austenitic grades. Joining DSS 2205 to austenitic 316L using a DSS filler metal offers a promising solution for improving SCC resistance in chloride environments. Gas tungsten arc welding (GTAW) was employed with ER 2209 filler metal, with heat input controlled to 1.3 kJ/mm, and multi-pass welding was performed. The resulting weld zone exhibited delta ferrite and austenite phases, with three distinct austenite morphologies: grain boundary, Widmanstätten, and intragranular. The heat-affected zone (HAZ) of the DSS showed coarse ferrite grains, while the HAZ of 316L displayed ferrite stringers within an austenite matrix. The weld exhibited higher hardness compared to the base metals, and its tensile properties were similar to those of the 316L base metal, though the weld's impact toughness was lower than that of both base metals, with fractures occurring on the 316L side during tensile testing. Electrochemical testing revealed that 316L had the best strength, followed by the weld, and then DSS 2205. In SCC testing, DSS 2205 and the weld

demonstrated excellent resistance, whereas 316L developed surface cracks. Overall, the dissimilar weld achieved good mechanical properties and excellent SCC resistance, with the austenite phase proving more electrochemically stable than ferrite. The DSS microstructure provided superior SCC resistance compared to the austenitic structure, indicating that the welding process and filler metal selection were suitable for joining these dissimilar materials.

2.1.1 FEM Model for Predicting Thermal History

Sepe R et al. [73] investigated welding process numerically using FEM thermal stress analysis. The numerical thermal-mechanical analyses were carried out using an uncoupled technique that comprised of two successive analyses: the first was used to compute the stress-strain fields using the previously computed temperature field as input data, and the second was used to predict the transient temperature field independently. Because it enables the decrease of the computational effort required by a linked temperature-displacement approach, this is a standard technique for these kinds of simulations. The element birth and death technique served as the foundation for the weld bead creation simulation. It was desirable to have a complete 3D model for the mesh.

Specifically, for the thermal analysis, 8-noded brick elements of type DC3D8 were chosen from the ABAQUS collection. Analysis because each node's temperature was taken into account as a distinct degree of freedom. Then, for the mechanical study, the C3D8 8-noded brick finite elements, which have three translational degrees of freedom for each node, were used instead of the DC3D8 while maintaining the same mesh size and shape. There was explicit modeling of the two weld beads. The initial part of the analysis involved deactivating the weld bead elements using the birth and death technique and then activating them in a way that simulated the production of weld beads during the welding process. The bead elements were eliminated from the analysis by applying a significant reduction factor to the element's stiffness to initiate the deactivation process. These components were joined with 26 sets of components that were gradually reactivated at certain intervals throughout the simulation. Reactivation was accomplished by deducting the reduction factor from the welding speed.

Ismail et al. [88] developed a 3D finite element model specifically for Gas Metal Arc Welding (GMAW) of aluminum alloy sheets. This model incorporates temperature-dependent properties and a moving Gaussian heat source. They validated the model against experimental measurements of weld bead profiles under different welding conditions, demonstrating its effectiveness and accuracy. The key points from the literature review are: Welding simulation

using finite element methods has been an active area of research since the 1970s, with pioneering work by researchers who developed an important double ellipsoidal heat source model for welding simulations that has been widely adopted. Numerical simulation has been successfully applied to various welding processes, including arc welding, friction stir welding, laser welding, and electron beam welding, to predict temperature fields and weld geometries. Thermal analysis is critical for welding simulations, with key phenomena such as heat conduction and convection losses needing to be modeled. Moving heat source models are crucial for accurately representing the welding arc, and Gaussian distributions are commonly used. To achieve accurate thermal modeling of welding, it is essential to incorporate temperature-dependent material properties. Mesh refinement in the weld zone is important to capture high-temperature gradients, and graded meshes are often used for this purpose. Experimental validation is crucial, often involving the comparison of predicted and measured weld bead geometries. Welding parameters like voltage, current, and speed significantly impact the temperature distribution and weld pool shape. Three-dimensional transient thermal models can provide insights into phenomena like through-thickness temperature gradients, which are difficult to measure experimentally. Finite element models can be used to study the effects of welding parameters and optimize processes. However, there are still challenges in accurately predicting weld geometries, with errors often in the 10-20% range when compared to experiments.

Pamnani et al. [89] conducted FEM simulations of the SMAW and A-GTAW processes for DMR-249A steel. It validates the models through experimental measurements and compares the residual stress profiles and mechanical properties of the two welding techniques. The aim is to establish A-GTAW as a viable alternative to SMAW for this particular steel, offering potential improvements in welding performance and structural integrity. The key aspects covered in the literature review are: DMR-249A is a low carbon high-strength low-alloy (HSLA) steel, featuring micro-alloying additions of vanadium (V), niobium (Nb), and titanium (Ti) for grain refinement. It possesses a microstructure characterized by fine equiaxed ferrite with less than 10% pearlite, making it suitable for use in the construction of ship hulls. While Shielded Metal Arc Welding (SMAW) is commonly employed for welding this material, it has certain limitations. An alternative is Activated Gas Tungsten Arc Welding (A-GTAW), a variant of GTAW that uses activated flux to increase penetration by up to 300% compared to conventional GTAW. Residual stresses in welding arise from incompatible internal permanent strains. Tensile residual stresses are detrimental as they facilitate crack propagation and fatigue

failure, whereas compressive residual stresses can be beneficial in preventing fatigue cracks. Numerical modeling, particularly finite element modeling (FEM), has been extensively used to predict thermal cycles and residual stresses in welds. Software like SYSWELD has proven effective for thermo-mechanical simulation of welding processes. In heat source modeling, the double ellipsoidal heat source distribution model is frequently employed, though other models such as semi-spherical and conical have been used depending on the specific welding process. Residual stress profiles can be experimentally measured using techniques like X-ray diffraction and ultrasonic methods. The welding thermal cycles induce various ferrite morphologies, such as grain boundary ferrite, Widmanstätten ferrite, and acicular ferrite, with the volume fractions of these phases influencing the final properties and residual stresses in the material. Key mechanical properties evaluated in welded joints include tensile strength, impact toughness, and hardness.

M Sohel et al. [90] conducted research to explore the temperature distribution during shielded metal arc welding (SMAW) of low carbon steel plates through both experimental measurements and numerical simulation and investigated that the Welding is a crucial material joining process, widely utilized in industry, with Shielded Metal Arc Welding (SMAW) being a popular method. Low carbon steel plates, such as those made from SA 516 Gr. 70, are commonly used for pressure vessels and other structural components due to their excellent mechanical properties. The residual stresses resulting from welding are significantly influenced by the heat distribution within the weldment, which can affect the integrity and performance of the welded structures. Previous work in this area has been limited, with only a few experimental studies focusing on the temperature distribution during multi-pass welding processes. However, advances in finite element modeling (FEM) have greatly enhanced the ability to analyze these temperature distributions. For instance, moving-mesh FEM has been employed to simulate temperature fields generated by moving heat sources, while Friedman developed thermo-mechanical FEM models specifically for welding applications. Additional studies have explored iterative procedures for nonlinear heat transfer analysis and have presented three-dimensional models of Gas Metal Arc (GMA) weld pools, including the effects of free surfaces and droplet impacts. In this study, both experimental and numerical methodologies were employed to investigate welding temperature fields. Experimentally, 8mm thick SA 516 Gr. 70 low carbon steel plates were used to create 45° and 60° V-groove joints with single and double pass welds. Temperatures were measured using thermocouples and a data logger to capture the thermal profiles. Numerically, ANSYS software was utilized for

three-dimensional nonlinear transient thermal FEM analysis, applying the Tsai heat source model and incorporating temperature-dependent material properties. The key findings of the study include the validation of numerical temperature predictions against experimental measurements, as well as the examination of the effects of weld geometry on temperature distributions. The transient temperature data obtained from this study can be instrumental in calculating residual stresses, thereby providing valuable insights for optimizing welding processes. Overall, this research contributes to the existing body of knowledge on welding thermal analysis and simulation techniques, offering a comprehensive approach to understanding and predicting welding-induced thermal behaviors.

Mr. Vodnala et al. [91] performed a design and transient thermal analysis of few welding using conical tool and investigated the effects of friction stir welding process parameters, The quality and properties of friction stir welds are significantly influenced by process parameters, including tool rotational speed, welding speed, and axial force. Higher rotational speeds typically result in increased peak temperatures and greater grain refinement. Optimizing these parameters is essential for maximizing tensile strength and other desirable properties in the weld. Tool Geometry Effects, The geometry of the FSW tool, particularly the pin profile and shoulder diameter, plays a crucial role in determining material flow and weld quality. Different pin profiles, such as cylindrical, threaded, and tapered, have distinct effects on the resulting weld. Threaded and square pin profiles are often found to produce superior joint quality, while the shoulder diameter affects the heat input and overall weld properties. Temperature distribution: During friction stir welding, peak temperatures typically reach 80-90% of the material's melting point. The temperature distribution is not uniform, it is generally higher on the advancing side compared to the retreating side of the weld. Both experimental measurements and Finite Element Analysis (FEA) modeling are commonly used to analyze the thermal history of the weld. Microstructure and Mechanical Properties, The friction stir welding (FSW) process results in the formation of fine, equiaxed grains in the stir zone through dynamic recrystallization. The grain size and dislocation density in this region significantly influence the mechanical properties of the weld, including tensile strength, hardness, and fatigue resistance. These properties are evaluated for various alloys and process parameters. Material Flow Behavior, The material flow around the FSW tool is complex and occurs in three dimensions. This flow behavior is studied using markers, modeling, and microstructure analysis. Proper material flow is critical to avoid defects, such as voids, and ensure a high-quality weld. Finite Element Analysis (FEA) software, like ANSYS, is commonly used to

predict temperature and stress distributions, while Computational Fluid Dynamics (CFD) modeling helps analyze material flow. Optimization Methods, Design of experiments approaches, such as the Taguchi method, are utilized to optimize FSW parameters. Analysis of Variance (ANOVA) is often used to determine the significance of different factors affecting weld quality. Emerging Research Areas, Recent research in FSW includes high-speed FSW, welding of ultrathin sheets, in-situ temperature measurement and control, and the development of hybrid and multi-pass FSW techniques. Key Conclusions, The literature review indicates that FSW process parameters, particularly tool rotational speed, have a substantial impact on weld quality and must be carefully optimized. The design of the tool geometry is also critical for ensuring proper material flow and successful weld formation. Temperature distribution and thermal history play significant roles in the evolution of microstructure and mechanical properties. Both experimental studies and modeling/simulation approaches are vital for gaining a comprehensive understanding of the FSW process and optimizing it for various applications. This extensive review highlights the major research trends and findings related to the FSW of aluminum alloys over the past decades, providing a strong foundation for further research and development in this field.

Syukri et al. [92] conducted research to explore thermal simulation of different welding speed and metal thickness for butt-joint welding with ANSYS and investigated issues such as welding deformation and residual stresses are critical, as they significantly impact the weld quality and strength, particularly in shielded metal arc welding (SMAW). Various studies have utilized finite element analysis (FEA) to explore the thermal effects and optimize welding parameters. The uneven heating and cooling during the welding process induce complex thermal stresses and strains, resulting in residual stresses and distortions, with the distribution of temperature being influenced by parameters like welding speed, plate thickness, and electrode size. Common deformations observed include longitudinal shrinkage, transverse shrinkage, angular distortion, and bowing distortion. FEA software, such as ANSYS, plays a crucial role in simulating these effects, allowing for precise calculation of distortions and residual stresses by accurately modeling the geometry, material properties, heat input, and boundary conditions. The simulations enable visualization of temperature distributions through contour plots on the welded plate, providing insights into how higher welding speeds can mitigate residual stresses and reduce the heat-affected zone, leading to narrower isotherms and shallower penetration. Thicker plates, on the other hand, tend to absorb more energy, resulting in lower peak temperatures and reduced overall residual stresses. The modeling of heat sources, often

represented by a Gaussian distribution of heat flux, depends on variables such as welding voltage, current, speed, and process efficiency. The simulation of moving heat sources is achieved by altering the location of the heat flux over time. Ultimately, these thermal simulations offer valuable insights into the optimization of welding parameters, aiming to enhance weld quality and minimize experimental efforts, with potential extensions to different joint configurations and welding processes in future research.

2.2 Problem Identification

Based on the literature survey, few research works have been conducted in the field of shielded metal arc welding (SMAW) of dissimilar materials. As per author's knowledge, none of the research work has been performed on SMAW of duplex 2205 and 316L stainless steel. Austenitic SS316L is primarily used in marine offshore oil rig platforms and ship construction. Recently, Duplex stainless steel has also been used in the marine sector because of its higher mechanical properties compared to austenitic stainless steel [2]. Therefore, welding of austenitic stainless steel is necessary for repairing ship components or parts. Some authors reported that SS 316L weldment exhibits lesser strength, durability, relative to duplex Stainless steel weldments [1].

Furthermore, the literature lacks studies that establish connections between experimental and computational fluid dynamics (CFD) simulation results, indicating an opportunity for interdisciplinary investigation. Additionally, the significance of this research extends beyond more experimental analysis. Transient thermal analysis based on the finite element method (FEM) may provide a clear idea of temperature distribution around the fusion zone, which can be validated with experimental results [91].

The marine environment presents unique challenges, such as high salinity, varying temperatures, and pressure conditions, which can affect the performance and longevity of welded joints. Strength, durability behavior are of prime importance in the marine industries [7].

Determining the optimal welding parameters (e.g., current, voltage, welding speed) to achieve high-quality welds with minimal defects and optimal mechanical properties. Understanding the microstructural changes that occur during the welding process and how these changes affect the overall performance of the welded joints in corrosive marine environments is necessary.

2.3 Aim & Objectives

The aim of this study is to evaluate and optimize the Shielded Metal Arc Welding (SMAW) process parameters for welding of Duplex Stainless Steel (DSS) 2205 and Austenitic Stainless Steel (SS) 316L by using different filler electrodes ER2209 and E316L-16, focusing on their suitability and performance in marine applications. The present research work seeks to enhance the understanding of how welding parameters influence the mechanical properties, and microstructural characteristics of these materials, to improve their durability and reliability in harsh marine environments.

- To successfully weld the dissimilar materials, duplex stainless steel 2205 and austenitic stainless steel 316L, using two different filler electrodes, ER2209 and E316L-16.
- To investigate the effects of process parameters, specifically welding current and welding speed, on responses such as weld deposition rate, weld seam width, and tensile strength.
- To examine the impact of different filler materials on the tensile behaviour, weld quality, and weld deposition rate of the weldments.
- To analyse the microstructural changes in SS 316L and DSS 2205 weldments and determine how various process parameters influence these changes.
- To identify the optimal shielded metal arc welding (SMAW) parameters, including current, voltage, and welding speed, to produce high-quality welds with minimal defects, and favorable mechanical properties.
- To compare the performance of DSS 2205 and SS 316L weldments in terms of mechanical properties, weld quality, and microstructural analysis.

CHAPTER 3

EXPERIMENTAL INVESTIGATIONS

This chapter discusses the welding techniques that involve using molten electrode metal to fill the weld gap and join workpieces. For welding stainless steel, especially marine-grade types, specialized electrodes that match the specific material are typically required. These electrodes are formulated to match the chemical composition of the base metal, ensuring the welded joint has the required mechanical properties. To ensure adequate heat input and prevent issues such as excessive heat distortion, grain growth, and metallurgical problems, various welding parameters are adjusted. The microstructure analysis involves examining the arrangement, composition, and properties of the small components within the weld. It also involves inspecting the present phases, the heat-affected zone, the grain structure, the solidification pattern, and identifying any imperfections. Techniques such as the optical metallurgical microscope are employed to examine these characteristics. The mechanical properties of the base metal and the welded samples are assessed, focusing specifically on compressive strength, and tensile strength. ANSYS software was used to conduct thermal analysis and explore temperature variations in different areas of the plate.

3.1 Work Materials

The base metals (BM) used in this study are Duplex 2205 and 316L stainless steel, sourced from special metals india and jaswant steel india. The filler materials used in the welding process were E316L-16 and ER 2209, sourced from Excellent Weld-Aids in West Bengal, India. The exact chemical composition of the base metals Duplex 2205 and AISI 316L is detailed in Table 3.1, while the chemical composition of the filler materials, electrode E316L-16, and ER 2209 is shown in Table 3.2. In addition to the welding materials, cutting-off wheels and flap discs are also utilized.

Table 3.1: Chemical composition of base alloy of SS316L [58] & DSS 2205 [75].

Base alloy	wt.% C	wt.% Mn	wt.% P	wt.% S	wt.% Si	wt.% Cr	wt.% Ni	wt.% Mo	wt.% N	wt.% Fe
SS316L	0.03	2.0	0.045	0.03	0.75	16.0	10.0	2.0	0.1	Bal.
DSS 2205	0.016	1.35	0.025	0.001	0.47	22.42	5.71	3.15	0.17	Bal.

Table 3.2: Chemical composition of filler materials E316L-16 [58] and ER 2209 [76].

Filler materials	C	Cu	Mo	Mn	Ni	Cr	Si	P	S	Fe
E316L-16	0.02	0.05	2.8	0.6	11.6	18.6	0.61	0.03	0.01	Bal.
ER 2209	0.023	0.10	3.02	1.57	8.65	23.02	0.56	0.022	0.001	Bal.

3.2 Experimental Setup

Shielded Metal Arc Welding (SMAW), also known as stick welding, is a process that uses a consumable electrode coated in flux to create the weld. An Essar arc welding machine was employed to weld the base metal using various types of filler electrodes, and appropriate personal protective equipment (PPE) was used throughout the experimentation.

Figure 3.1 below provides a pictorial view of the SMAW experimental setup, while Table 3.3 details the specifications of the arc welding machine.

Figure 3.1: Pictorial view of SMAW welding setup

Table 3.3: Specification of the SMAW machine

Welding Type	Arc
Output Current	30 - 250 A
Input Power	6 - 12 kVA
Supply Voltage	230 V
Phase	Single Phase
Automation Grade	Automatic

3.3 Welding Fixture

A welding fixture is a support or work-holding device used to precisely position and secure materials in a specific location or orientation. For this present study, the fixture is designed to hold the workpiece securely. Mild steel is used as a support for the base metal, which is secured in place with stainless steel holding clips. Additionally, a bench vice is employed to fasten the mild steel plate firmly. Figure 3.2 displays the pictorial view welding fixture.

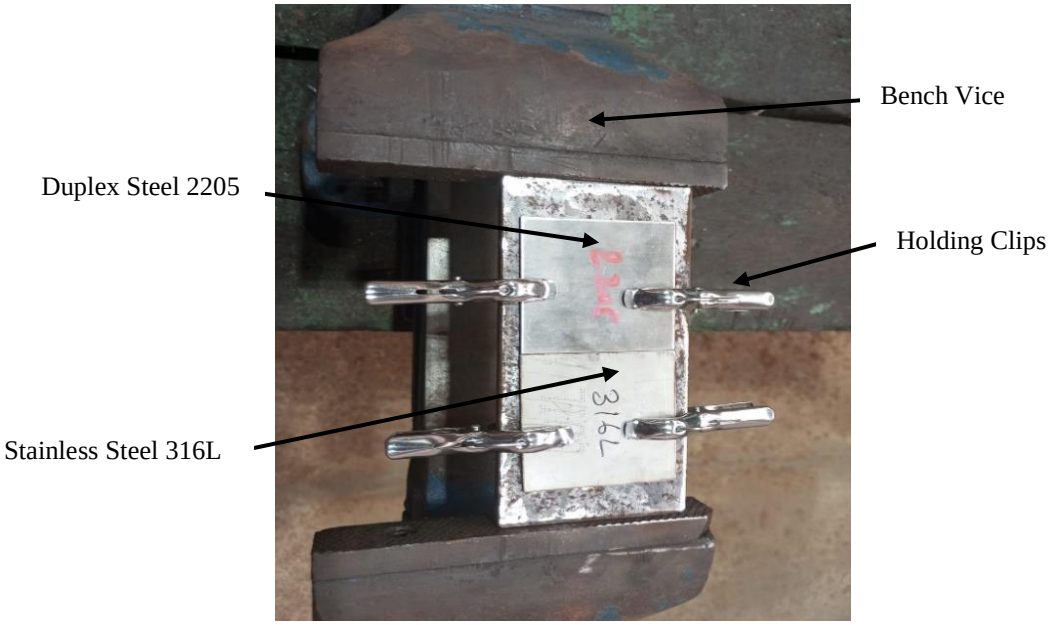

Figure 3.2: Pictorial view of welding fixture

3.4 SMAW Procedure

Figure 3.3 illustrates the steps involved in setting up and operating an arc welding process. The first step is to ensure that the main power supply is available and functioning, as welding

equipment requires a stable power source to operate effectively. Next, the welding machine is connected to the main power supply, ensuring all electrical connections are secure and correctly set up. The work clamp, also known as the ground clamp, is then connected to the workpiece to complete the electrical circuit required for welding. The appropriate electrode for the welding job is selected, with the choice depending on factors like the type of material being welded, the desired weld quality, and the specific welding process being used. The type and diameter of the electrode are chosen based on the welding requirements, as the type influences the properties of the weld, while the diameter affects the current needed and the deposition rate. The welding machine's output settings are adjusted according to the selected electrode and work piece, typically involving setting the voltage and amperage. The amperage is set to a level appropriate for the electrode type and the thickness of the material being welded, as proper amperage settings are crucial for achieving good weld penetration and quality. The selected electrode is inserted into the electrode holder, which is then connected to the welding cable, completing the setup. Finally, the welding arc is initiated by striking the electrode against the work piece, generating intense heat that melts the electrode and the work piece to form the weld.

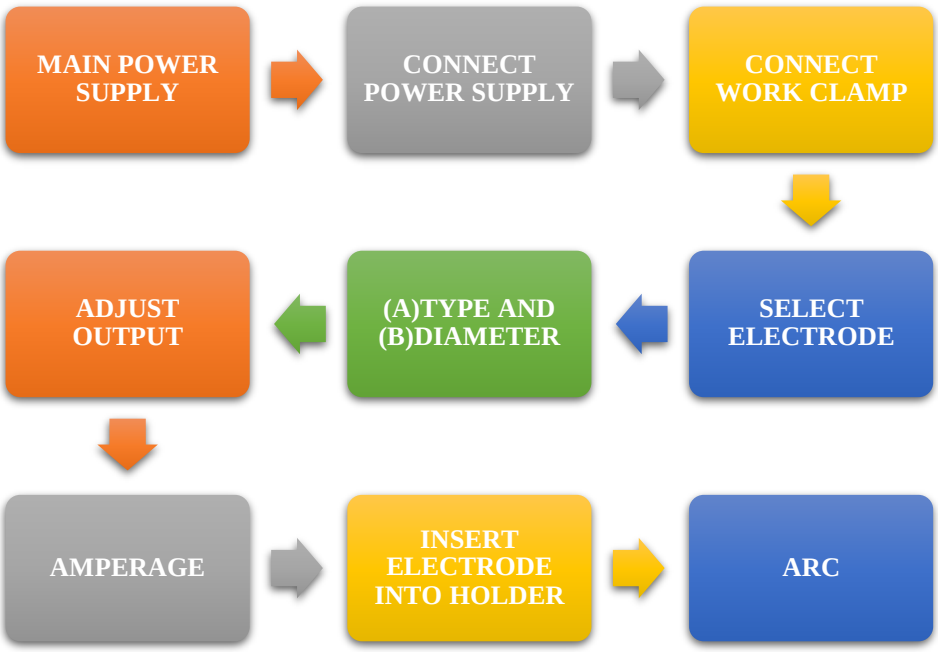

Figure 3.3: Flow chart of SMAW procedure

3.5 Techniques Adopted for Welding of DSS 2205 & SS316L

Using a cut-off wheel, the stainless steel Duplex 2205 and SS316L are sliced into plates measuring 60 mm by 60 mm with a thickness of 2 mm. Three sets of samples, each with identical dimensions, were prepared to create welding specimens. Emery paper is employed to smooth the edges of the steel plate, ensuring a clean surface before welding. Duplex 2205 and SS316L stainless steel are welded using the SMAW method with different electrode filler materials. In direct-current straight polarity, the workpiece is positively charged while the electrode carries a negative charge.

The samples are welded using a single square groove weld with butt joints, performed in a down-hand position at a 70-degree angle. A single pass is used to minimize the overall heat input to the base material. This approach significantly reduces the risk of distortion and effects in the heat-affected zone (HAZ). Welding safety measures ensured that PPE was properly worn, adequate ventilation was provided, and safe work procedures were consistently followed to minimize potential risks. Figure 3.4 provides a detailed illustration of the specific welding technique.

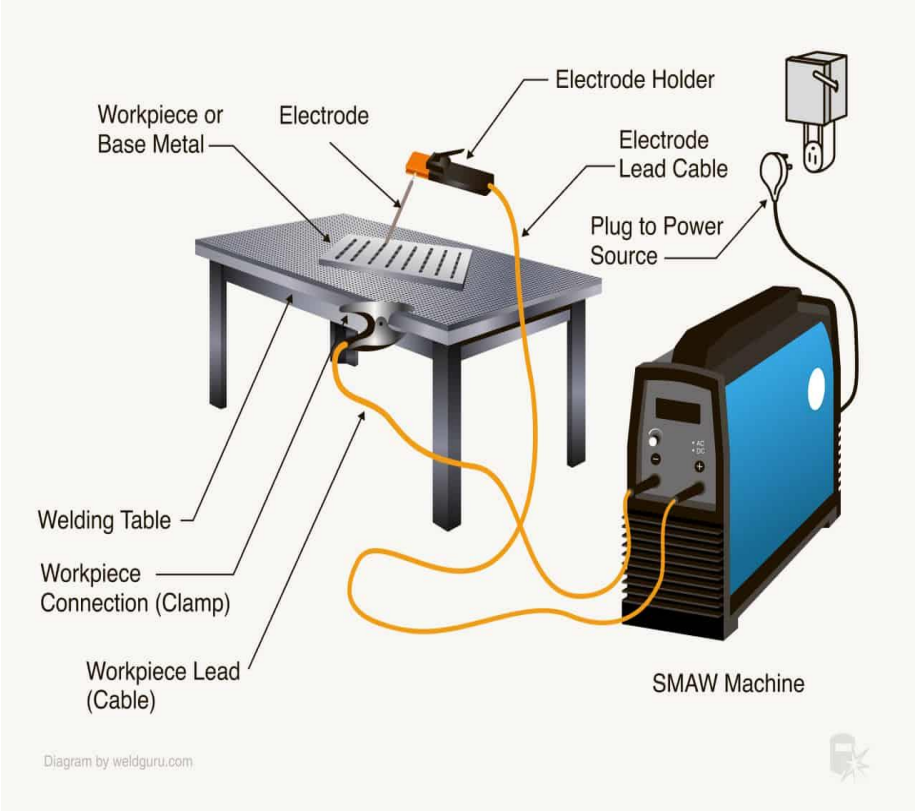

Figure 3.4: Schematic of SMAW welding technique [77].

The welding input by using an electrode of E316L-16 and ER2209 at various currents has been given in Table 3.4.

Table 3.4: Welding input by using an electrode of E316L-16 and ER2209 at various current

Sample, ID	Welding current, A	Arc voltage, V	Weld length, mm	Time, min	Travel speed, mm/min	Heat input, KJ/mm
A1	80	24	60	0.316	189.873	0.606
A2	90	24	60	0.278	215.827	0.600
A3	100	24	60	0.239	251.046	0.573
B1	80	24	60	0.347	172.910	0.666
B2	90	24	60	0.291	206.185	0.628
B3	100	24	60	0.259	231.660	0.621

Once the welding parameters have been successfully applied, the welded specimen is prepared for further characterization. Figure 3.5 displays the sample of DSS 2205 & SS 316L plates before welding, while Figures 3.6 and 3.7 show the plates after welding, using electrodes (a) ER2209 and (b) E316L-16, respectively.

.

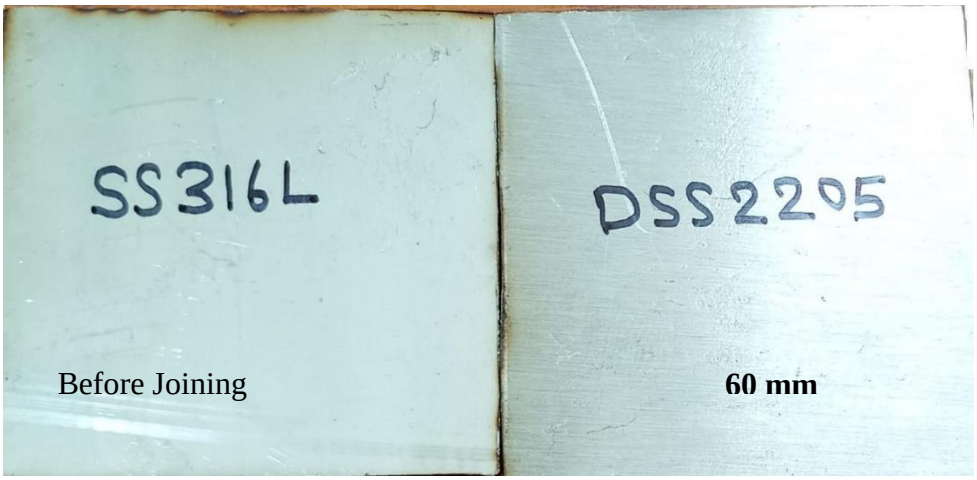

Figure 3.5: Sample of DSS 2205 & SS 316L plate before welding

Figure 3.6: Sample after welding by using an electrode (a) ER2209

Figure 3.7: Sample after welding by using an electrode (b) E316L-16

To calculate the heat input in SMAW, it is essential to measure the amount of energy transferred to the workpiece per unit length by the welding arc [78]. This can be achieved by applying the following equation.

$$\text{Heat input (HI)} = \frac{\text{V} \times \text{I} \times 60}{1000 \times \text{S}}$$

Where, HI is heat input in (kJ/mm), V is Arc voltage in volts, A is welding current in ampere, and S is travel speed in (mm/min).

3.6 Methodology

The flow chart shown in figure 3.8 outlines the process of studying the welding characteristics of dissimilar materials. This initial step involves choosing the materials that will be welded togethers. The selection is critical as the properties of the materials, such as their melting points, thermal conductivity, and mechanical properties, will influence the welding process and the final outcome. After selecting the materials, the next step is to choose an appropriate welding process. This decision is based on the types of materials, their thickness, and the desired properties of the final weld. Common welding processes include MIG (Metal Inert Gas) welding, TIG (Tungsten Inert Gas) welding, and arc welding, among others. Now the third

steps involves the chosen materials are welded using the selected process. The welding parameters, such as temperature, welding speed, and filler materials, are carefully controlled to ensure a high-quality weld. In fourth steps once the welding is complete, the welded materials are tested to evaluate their mechanical properties and welding characteristics. This includes checking for strength, ductility, hardness, and any defects such as cracks or voids in the weld. This is the fifth steps and it involves analyzing how well the different materials bonded during the welding process. Dissimilar materials can present challenges due to differences in their thermal expansion rates, melting points, and other properties. The study aims to understand these challenges and how they affect the quality and durability of the weld. Finally, the results from the mechanical testing and study of welding characteristics are compiled and analyzed. Conclusions are drawn regarding the effectiveness of the welding process for the selected materials, potential improvements, and the implications for practical applications. This step is crucial for providing recommendations for future welding projects and for optimizing welding processes. Overall, this flowchart provides a systematic approach to studying and optimizing welding processes, particularly when dealing with dissimilar materials.

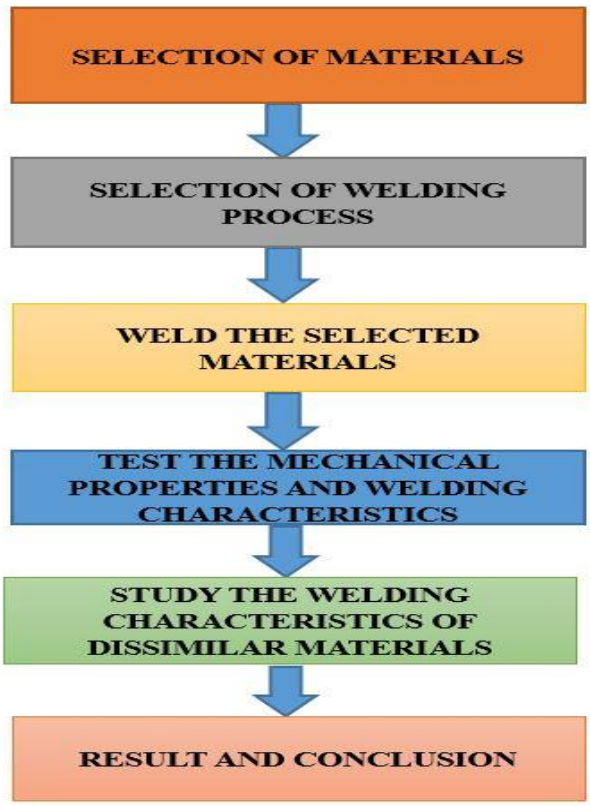

Figure 3.8: Flow chart showing methodology followed for the present work.

3.7 Weld Deposition

The process of adding filler material to a junction while welding to form a weld bead is known as "weld deposition. Weld deposition has been measured by the wensar high precision electronic balance. The weight of both the base metal has been separately measured before welding using this device and also the weight of the base metal has been measured after welding using this device then the weld deposition has been calculated using the given below formula and the final calculated weld deposition has been shown in the table 3.6. Figure 3.9 shows the pictorial view of the electronic balance device and Table 3.5 shows the specification of the wensar electronic balance device.

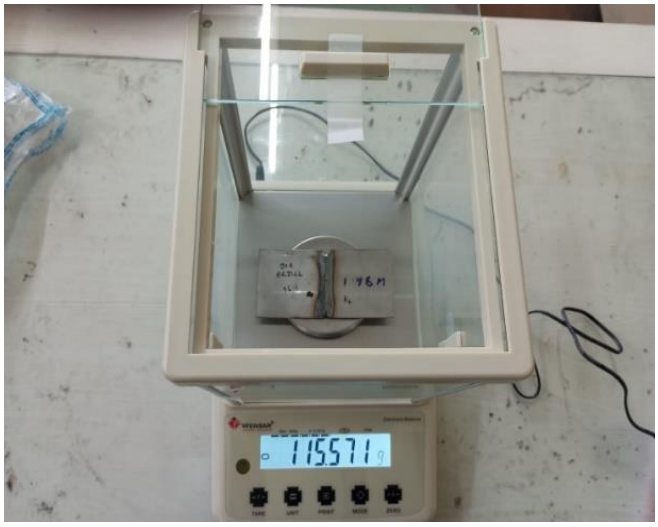

Figure 3.9: Pictorial view of electronic balance device

Table 3.5: Specification of wensar electronic balance

Type	**Electronic Balance**
Temperature Range (°C)	15 to 25
Power Supply	AC 220V / 50-60 Hz
Weight	10 kg
Max. (Capacity)	520g
Min. (Capacity)	0.1 g
Pan Size (mm)	80 mm Ø

The formula used to calculate the weld deposition:

$$\text{Weld Deposition}(\%) = \frac{\text{Weight after welding} - \text{Weight before welding}}{\text{Weight after welding}} \text{ X } 100$$

Table 3.6: Weld deposition of specimen at various current.

Sample	Welding current (A)	Arc voltage (V)	Weld deposition (%)
A1	80	24	2
A2	90	24	2.4
A3	100	24	1.5
B1	80	24	1.8
B2	90	24	2.2
B3	100	24	2.1

3.8 Characterization Techniques

After successfully welding DSS 2205 and SS 316L stainless steel, the impact of varying current and electrode types on the microstructure and mechanical properties of the welded specimen has been analyzed. Before any characterization is performed, the welded samples are visually inspected for surface flaws, cracks, or irregularities. After the visual inspection, the prepared samples underwent a series of characterization procedures.

3.8.1 Microstructural Evolution

The Optical microscopic analysis are conducted to examine the overall morphology of the welded samples. Each welded specimen has been prepared according to ASTM E407 standards for microstructure analysis. The samples' surfaces and cross-sections are mounted with epoxy resin and polished to a mirror finish using various grades of emery paper, cloth, and diamond polishing. The polished samples were etched with Kelling's reagent (5 grams of CuCl2, 40 ml of HCl, and 40 ml of alcohol) following standard metallographic procedures. It is used to examine the fusion zone (FZ), heat-affected zone (HAZ), and any surface imperfections, aiding in the identification of features such as inclusions, surface cracks, or weld defects.

3.8.2 Tensile Test

Transverse tensile specimens (with length perpendicular to the welding direction) are prepared using electrical discharge machining (EDM) and evaluated according to the ASTM E8 standard for tensile tests at room temperature. The dimensions and design of the samples for tensile tests are carried out at room temperature. A cross-head speed (displacement rate) of 1 mm/min was selected for the tensile test. The tensile tests at room temperature are performed using a 50 kN, Instron 8862 tensile testing machine. Figure 3.10 displays the dimensions required for preparing a tensile specimen.

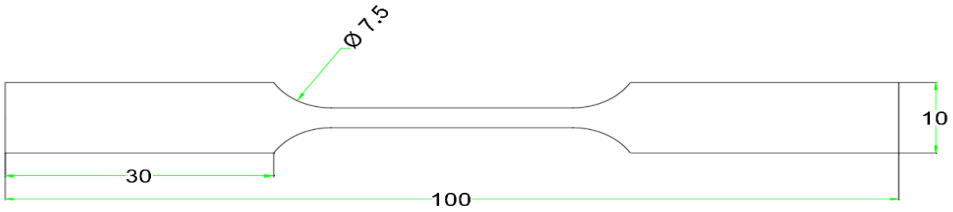

Figure 3.10: Dimension of a tensile welded specimen prepared by WEDM

3.9 Infrared Thermal Imager

Figure 3.11 represents a thermal imaging camera, specifically a Fluke brand thermal imager. This type of device is commonly used in various fields, including electrical and mechanical inspections, building diagnostics, and preventive maintenance, to detect heat patterns and temperature variations in objects and environments. The camera has a screen that displays the thermal image or infrared data captured by the device. The image shows some fingerprints or smudges on the screen, which is common with touchscreens or devices used frequently in the field. Below the display, there are several buttons for navigating the camera's menu and settings. These buttons are used to adjust parameters, switch between modes, and manage saved data.

Thermal imaging cameras are used to visualize temperature differences across surfaces. They are valuable in detecting issues like overheating components, insulation gaps, leaks, and more. The thermal data can help identify problems that are not visible to the naked eye, making these devices essential tools in maintenance, inspection, and diagnostic tasks. Table 3.7, displays the specification of fluke ti450 thermal imager camera.

Figure 3.11: Pictorial view of fluke ti450 thermal imager camera

Table 3.7: Specification of fluke ti450 thermal imager camera

Temperature	-10 °C to +50 °C
AC Operation	110 V ac to 220 V ac, 50/60 Hz
Infrared spectral band	7.5 µm to 14 µm (long wave)
IR-Fusion Technology	100 %, 75 %, 50 %, 25 % IR plus full visible on camera
Standard Infrared Lens Spatial Resolution (IFOV)	1.31 mRad
Visual (Visible Light) Camera, Type	Industrial performance 5.0 MP

3.10 Transient Thermal Analysis

A finite element model of the object under examination and the temperature distribution over time are the two steps in the transient thermal analysis procedure in ANSYS. This process consists of the following key steps: (a) creating the geometry; (b) meshing; (c) assigning materials; (d) defining the boundary conditions; and (e) computing the solution. These procedures result in the generation of a finite element model, which makes it possible to acquire the temperature distribution over time and analyze transient thermal behavior. The thermal

analysis conducted in this study included all necessary analyses within the transient thermal domain and was conducted using the student edition of ANSYS 2024 R1.

3.10.1 Finite Element Modelling for DSS 2205 and SS 316L.

In transient thermal analysis, the temperature field (T) of a welded plate depends on time (t), and thermal conduction will occur in the metal. The governing partial differential equation for three-dimensional transient heat conduction with internal heat generation during welding is described by the thermal equilibrium equation provided in [79].

$$\frac{\partial}{\partial x}\left(K_x \frac{\partial T}{\partial x}\right) + \frac{\partial}{\partial y}\left(K_y \frac{\partial T}{\partial x}\right) + \frac{\partial}{\partial z}\left(K_z \frac{\partial T}{\partial x}\right) + Q = \rho c \left(\frac{\partial T}{\partial x}\right) \tag{3.1}$$

Where T represent the temperature (°C), K stand for thermal conductivity (W/m °C), c denotes the specific heat (J/kg °C), q represents the density (kg/m3), t represents the time (min), Q represents the rate of heat generation per unit volume (W/m3). Boundary conditions, the specific heat flow acting over the surface will be that of surface convection and radiation is given by [79].

$$\left(K_n \frac{\partial T}{\partial n}\right) = h\left(T_w - T_f\right) + \varepsilon\sigma\left(T_w^4 - T_f^4\right) \tag{3.2}$$

Where h is the heat transfer coefficient at the model surface, Tw is the temperature of the model surface, T_f is the temperature of the surrounding, e is the radiation coefficient of the black body, and r is the Stefan-Boltzmann constant. The calculation of heat input in SMAW involves determining the quantity of energy transmitted to the workpiece per unit length by the welding arc. This is done by applying the following equation [80].

$$Heat\ input\ (HI) = \frac{V \times I \times 60}{1000 \times S} \tag{3.3}$$

Where HI is heat Input (kJ/mm), V is Arc voltage in volts, A is Welding Current in ampere, and S is Travel speed (mm/min). The heat Flux Equation can be calculated using this equation

$$\text{Heat Flux}(q) = H/S \times L \tag{3.4}$$

Where q is Heat Flux in (W/mm2), H = Heat Input in joules/ mm, S = welding Speed in mm/s, L = length of the weld in mm. This equation relates the heat flux to the heat input, length of the weld, and welding speed. The heat flux is a measure of the amount of heat energy transferred per unit area per unit time, the heat input is the total amount of energy delivered to the weld area per unit length of the weld, and it is determined by the welding process parameters. Assuming that the heat input is uniformly distributed throughout the length of the weld and there are no heat losses, the equation enables the calculation of the heat flux, which can be utilized to approximate the temperature distribution in the material.

CHAPTER 4

RESULT AND DISCUSSION

This chapter details the experimental findings from metallurgical studies, as well as mechanical and weld tests conducted under both welded and thermal conditions. Both tabular and graphical results are provided, along with a discussion of the findings for welds with different joint designs.

4.1 Weld Deposition

In shielded metal arc welding the process of adding filler material to a junction while welding to form a weld bead is known as "weld deposition." Figure 4.1 shows the relationship between welding current (A) and weld deposition (%) for two different types of electrodes ER2209 and E316L-16.

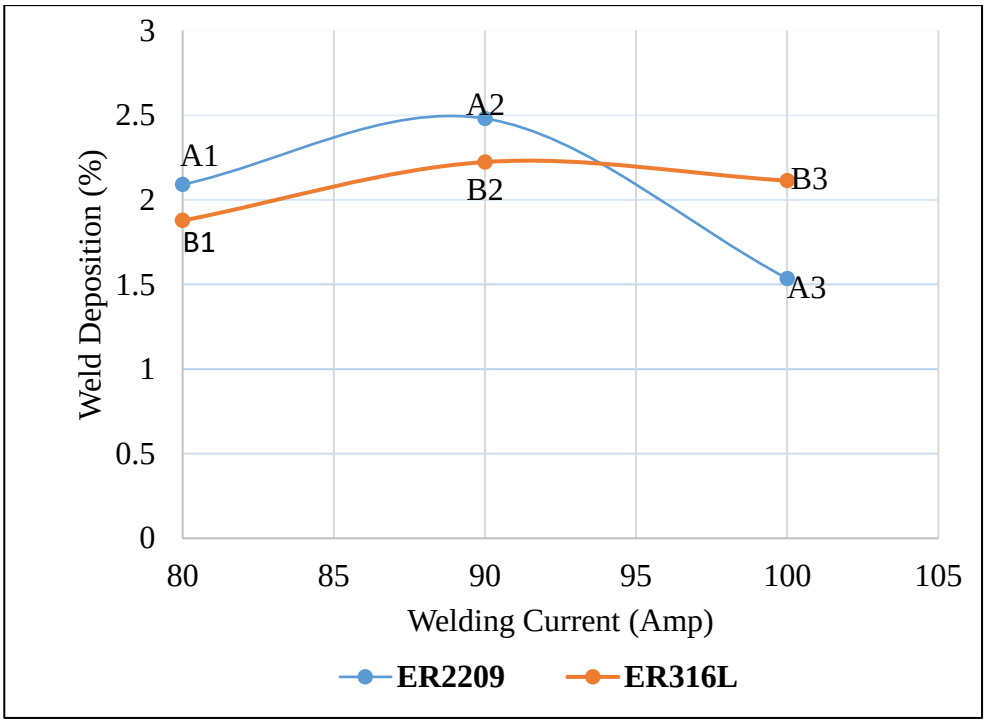

Figure 4.1: Weld deposition versus current (A) for two different types of electrode

Graph illustrates the relationship between current (in amperes) and weld deposition (%) for two filler metals ER2209 and ER316L. The x-axis indicates the current, ranging from 80 to 100 amps, while the y-axis shows the weld deposition. The weld deposition begins at approximately 2% at 80 amps. This is likely due to an increase in the heat input (HI), which

promotes better melting and deposition of the filler material. Using equations 3.3 & 3.4, as the current (I) increases, HI increases (assuming voltage V and speed S remain constant), resulting in higher heat input and thus more weld deposition. Table 4.1 displays the weld deposition of specimen at various currents.

Table 4.1: Weld deposition of specimen at various currents.

Sample	Welding current, (A)	Arc voltage, (V)	Weld deposition (%)
A1	80	24	2
A2	90	24	2.4
A3	100	24	1.5
B1	80	24	1.8
B2	90	24	2.2
B3	100	24	2.1

At 90A, the weld deposition reaches its peak (about 2.5%). This is due to an optimal current where the heat input is sufficient to maximize deposition without causing issues like excessive heat or instability. Beyond 90A, the deposition decreases significantly due to excessive heat causing weld pool instability or increased arc blow, leading to a less efficient deposition process. Similarly for E316L-16, the deposition reaches up to 1.9% at 80 amps. As the current rises to 90 amps, the deposition increases to about 2.2% and at 100 amps it decreases to 2.1%. ER2209 shows a sharper increase and decrease in deposition with changes in current, suggesting it's more sensitive to heat input variations. Whereas ER316L exhibits a more gradual change, indicating it might tolerate a wider range of heat input without significant loss in deposition efficiency. For both materials, optimal deposition occurs where heat flux is balanced enough to melt filler material effectively but not so high as to cause defects.

4.2 Weld Seam Width

Weld seam width is critical for understanding the quality of a weld. It helps in identifying potential issues like improper fusion, excessive heat input, or the presence of harmful phases that could compromise the weld's strength. This analysis ensures that the weld meets the required specifications and standards for the intended application. The width of the fusion zone (the distance between the boundaries where the base materials have melted and fused) is

measured. This is often done using optical microscope image analysis software that can precisely measure the dimensions of weld width. figure 4.2 and table 4.2 represents the weld seam width of all the specimens at different current.

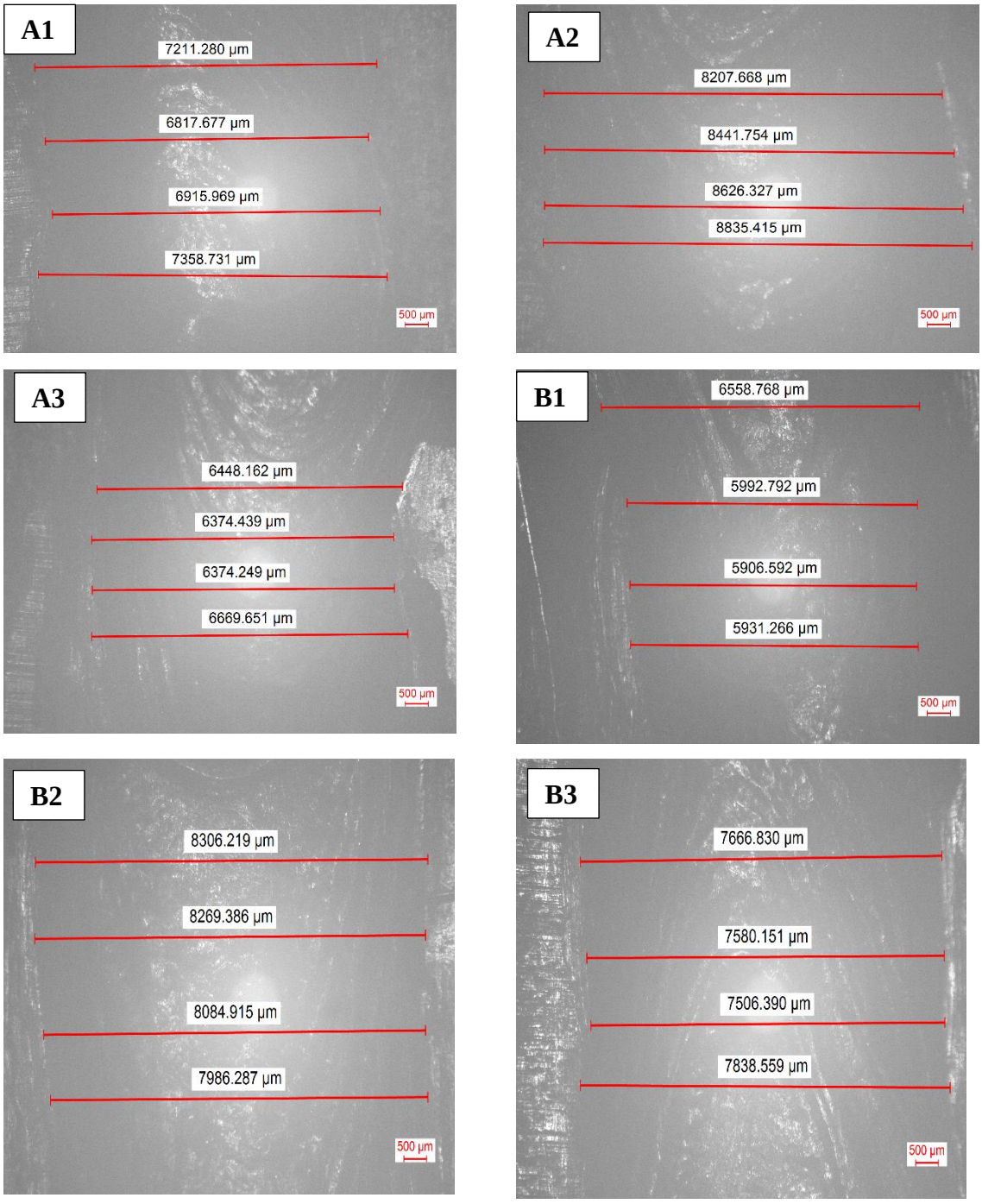

Figure 4.2: Weld seam width of all the specimens at different current

Table 4.2: Weld seam width of all the specimens at different current

Sample	Weld seam width (µm)	Current (A)
A1	7075.914	80
A2	8527.791	90
A3	6466.575	100
B1	6097.354	80
B2	8161.701	90
B3	7647.982	100

Graph represents the relationship between the welding current (A) and the weld seam width (µm) for two different electrodes ER2209 and E316L-16.

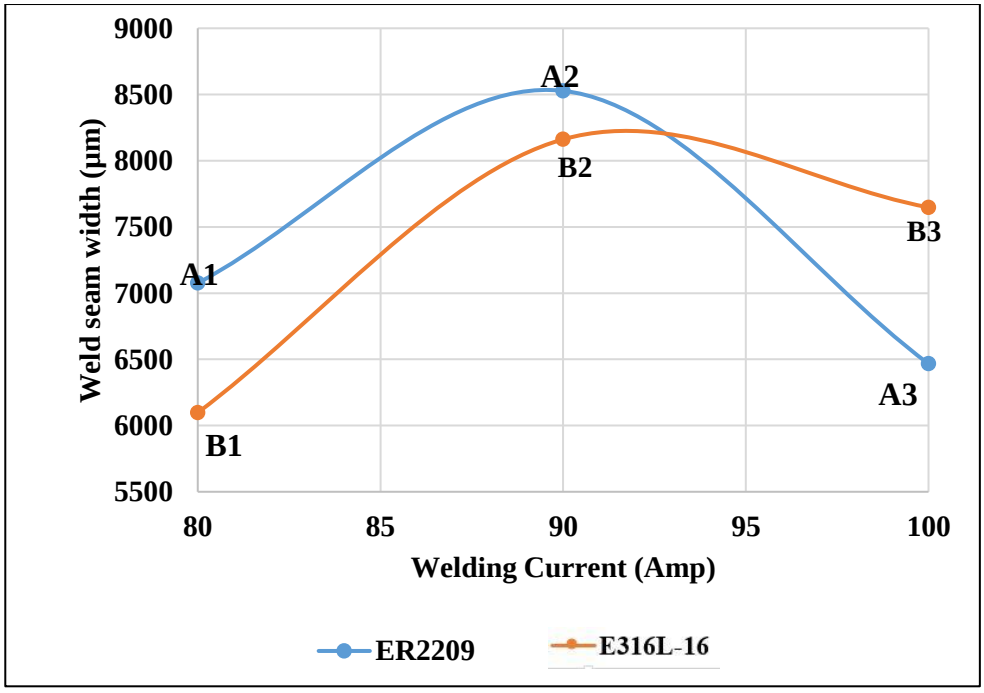

Figure 4.3: Weld seam width of all the specimens at different current

Graph illustrates the variation in weld seam width with welding current for two types of electrodes, ER2209 and E316L-16. For ER2209, the weld seam width increases from 7000 µm to a peak of 8500 µm as the current rises from 80A to 90A, then decreases to 6000 µm at 100A. Similarly, for E316L-16, the weld seam width increases from 6000 µm to a peak of 8000 µm as the current rises from 80A to 90A, then decreases to 7000 µm at 100A. As the welding

current increases from 80A to 90A, both electrodes show an increase in weld seam width, indicating higher heat input leading to a wider seam. However, as the welding current increases from 90A to 100A, both electrodes exhibit a decrease in weld seam width. This decrease may be due to an increase in welding speed (S) at higher currents, which reduces the heat input per unit length and consequently the weld seam width. ER2209 shows a more pronounced peak and drop in weld seam width, indicating it is more sensitive to changes in welding current, while E316L-16 exhibits a steadier increase and decrease, indicating more consistent behavior with varying currents.

4.3 Tensile Strength

Tensile testing was performed on all the welded samples to study the relationship between applied stress and strain which is shown in Figure 4.4. Each curve represents the stress-strain behavior of a specific sample under certain conditions. The x-axis represents the tensile strain, which is the deformation or elongation of the material as a percentage of its original length. The y-axis represents the tensile stress, which is the force per unit area applied to the material.

After the initial linear portion of each curve (elastic region), as the stress increases, the material reaches the yield point and the curves exhibit a nonlinear behavior indicating plastic deformation. Beyond the yield point, the material enters the plastic region. In this region, the graph shows a gradual and nonlinear increase in stress with strain. The material keeps undergoing plastic deformation, and the strain increases at a relatively steady rate. This is the permanent deformation that occurs when the material is subjected to stress beyond its elastic limit. As we know the ultimate tensile strength (UTS) is the maximum stress that a material can withstand. Figure 4.4 represents the curve for A2, which shows higher ultimate stress than the remaining respective specimens indicating that this material is better strength compared to others. After reaching the ultimate tensile stress (UTS) point, stress starts to decrease while the strain continues to increase, indicating the onset of necking and eventual fracture. The sharp drop in each curve after the peak indicates the point of fracture. Ductility is determined by the

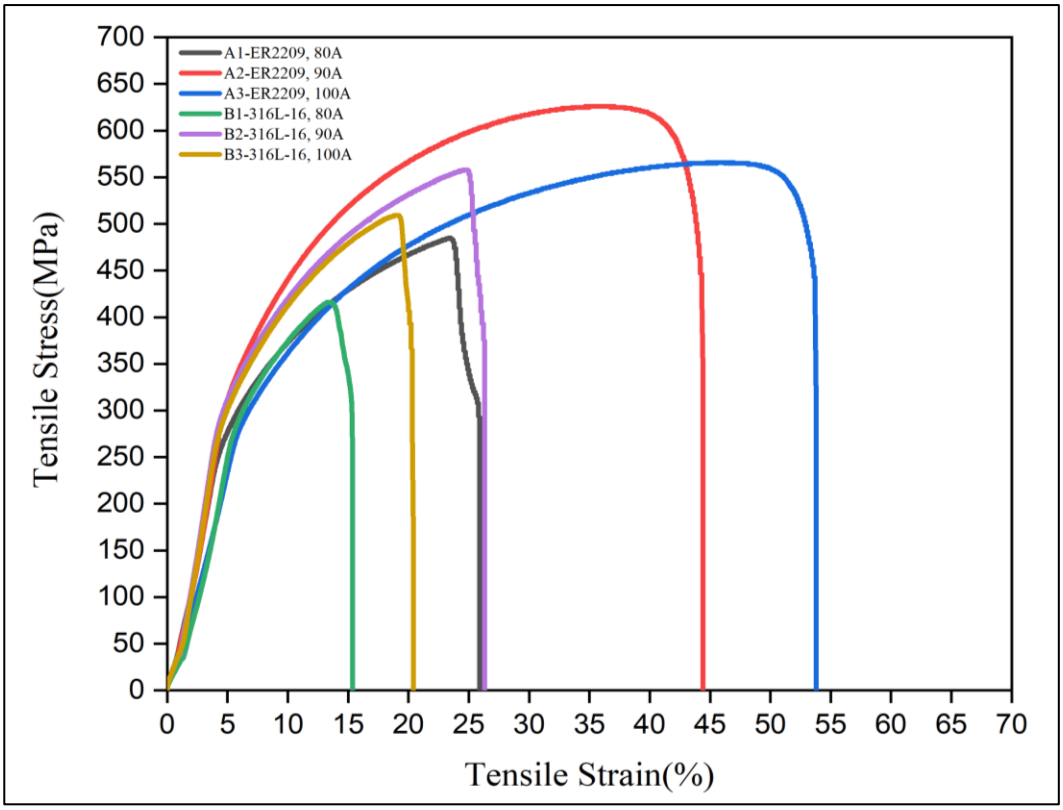

Figure 4.4: Tensile stress versus strain graph of welded sample at different current

strain at fracture, which represents the maximum strain the material can endure before failing. It indicates how much a material can stretch before breaking. It has been observed that the curve for A3 shows high ductility, stretching to around 55% strain. Additionally, the area under each curve represents the strain energy, which is the amount of energy the material absorbs before it fails. It indicates the material's toughness, materials with larger areas under their curves can absorb more energy before breaking, suggesting higher toughness. It has been observed that the A2 is showing higher area compared to others means it is showing higher strain energy compared to others so it has better toughness than the other respective specimens. The detailed tensile results, including yield strength, ultimate tensile strength, and elongation percentage, are presented in Table 4.3.

The tensile test results show that the ultimate tensile strength of ER 2209 welded sample initially increases from to 485 N/mm² to 626 N/mm² as the welding current increases from 80 A to 90 A. However, with a further increase in current from 90 A to 100 A, the ultimate tensile strength decreases from 626 N/mm² to 566 N/mm². The ultimate tensile strength of ER 316 L welded materials initially increases from 416 N/mm² to 558 N/mm² as the current increases from 80 A to 90 A, but then decreases from 558 N/mm² to 509 N/mm² as the current rises from

90 A to 100 A. It has been observe that as the welding current increases from 80 A to 90 A, the heat input to the weld increases, leading to deeper weld penetration. This is because higher current generates more heat, which melts more of the base metal, allowing the weld pool to penetrate deeper into the material. The initial increase in ultimate tensile strength (UTS) observed in both ER2209 and ER316L samples suggests that the increased penetration at these currents leads to better fusion and a more robust weld, which can handle higher loads before failing.

Furthermore, when the current is further increased from 90 A to 100 A, the weld penetration depth can continue to increase initially due to the higher heat input. However, there is a point beyond which additional current can lead to issues such as excessive heat input, resulting in problems like excessive dilution, or excessive reinforcement, which might not contribute positively to the mechanical properties. The observed decrease in UTS from 90 A to 100 A for both ER2209 and ER316L may indicate that while penetration depth could still be increasing, other factors are negatively affecting the mechanical properties. These includes excessive welding current can lead to overheating and grain growth, which weakens the weld, as well as increased defects and porosity due to higher evaporation of alloying elements, reducing the weld's overall strength. Therefore, while the weld penetration depth generally increases with an increase in welding current, the relationship is not linear beyond a certain point. The optimal penetration depth that contributes positively to weld strength and quality is typically achieved at an intermediate current level (in this case, around 90 A), beyond which further increases in current may not be beneficial and can even be detrimental due to the negative effects of excessive heat input. The increase in UTS from 80 A to 90 A can be attributed to improved fusion and microstructure refinement. However, the subsequent decrease from 90 A to 100 A is likely due to overheating, grain growth, potential phase transformations, and increased residual stresses, which can all contribute to a reduction in tensile strength. This pattern is observed for both ER2209 and ER316L, indicating that these materials have optimal welding conditions that maximize their tensile strength, beyond which the properties degrade. It has been investigated that the ER2209 materials (A-series) generally show higher tensile strength and ductility compared to 316L-16 (B-series), as indicated by the higher and more extended curves. Figure 4.4 shows the tensile stress versus strain graph of welded sample at different current and Table 4.3 displays the Ultimate tensile, yield stress, and elongation of all specimens at different currents.

Table 4.3: Ultimate tensile, yield stress, and elongation of all specimens at different currents

Sample	Yield stress (N/mm^2)	Elongation (%)	Ultimate Tensile stress (N/mm^2)
A1	620	30.6	626
A2	485	23.2	485
A3	544	32.6	566
B1	555	23.4	558
B2	416	12.57	416
B3	509	19.05	509

4.4 Measurement of Temperature Using Infrared Thermal Imager

Figure 4.5 illustrates the thermal profile recorded during welding with an ER2209 filler at a current of 80A. The highest temperature observed is 2936.6°C, while the lowest is 23.3°C. The thermal image emphasizes the heat-affected zone (HAZ), with a central hot spot representing the weld pool. The color scale, ranging from dark blue (cooler areas) to red (hottest areas), displays the heat distribution. Figure 4.6 presents the thermal profile for welding with ER2209 at 90A. The highest recorded temperature is 2280.2°C, while the lowest is 23.3°C. Although the heat distribution pattern is similar to that in Figure 4.5, the maximum temperature is lower, suggesting potential variations in thermal conductivity or heat dissipation.

Figure 4.7 displays the temperature distribution for welding with ER2209 at 100A. The highest temperature recorded is 1906.4°C, while the lowest is 24.3°C. The peak temperature appears lower than in previous images, which could indicate variations in heat input or potential measurement variations. Figure 4.8 presents the thermal profile for welding with E316L-16 filler at 80A. The maximum temperature achieved is 3056.2°C, while the minimum is 25.2°C. Although the thermal distribution is similar to that in previous figures, it features a distinct color pattern and a higher peak temperature, suggesting variations in thermal behavior between the ER2209 and E316L-16 fillers.

Figure 4.9 displays the temperature range indicated by the color scale on the right, which spans from a minimum of 22.9°C to a maximum of 2386°C. The welding process is performed at a current of 90A. The image reveals a concentrated heat zone, with the hottest area marked by a cross labeled "HI." The color gradient transitions from white/red (indicating the hottest areas) to blue (indicating cooler areas), illustrating the temperature gradient.

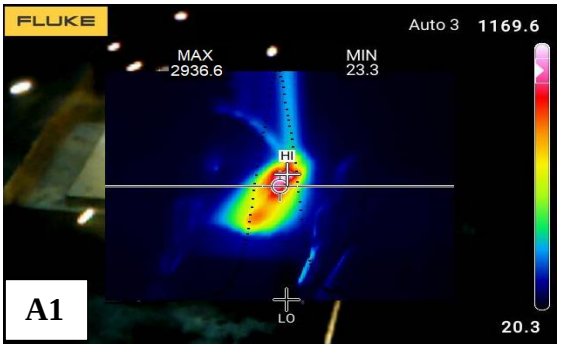

Figure 4.5: Temperature at 80A welded by ER2209

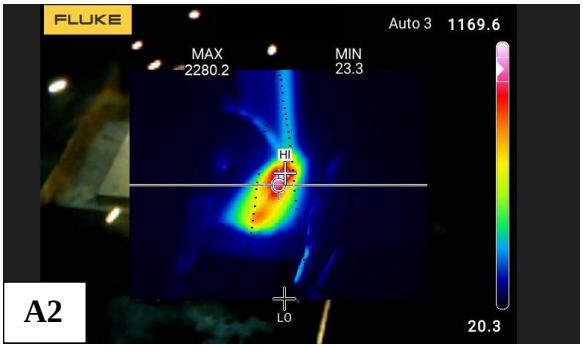

Figure 4.6: Temperature at 90A welded by ER2209

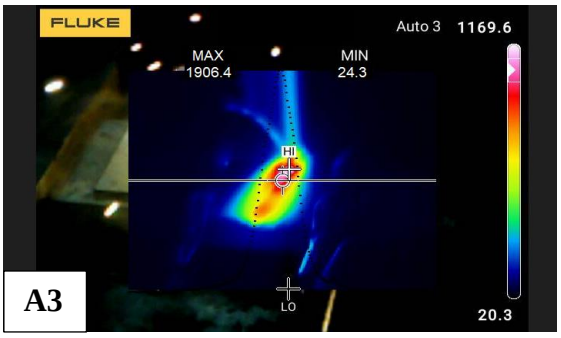

Figure 4.7: Temperature at 100A welded by ER2209

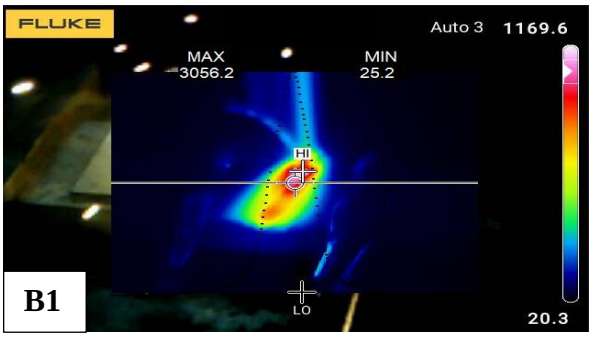

Figure 4.8: Temperature at 80A welded by E316L-16

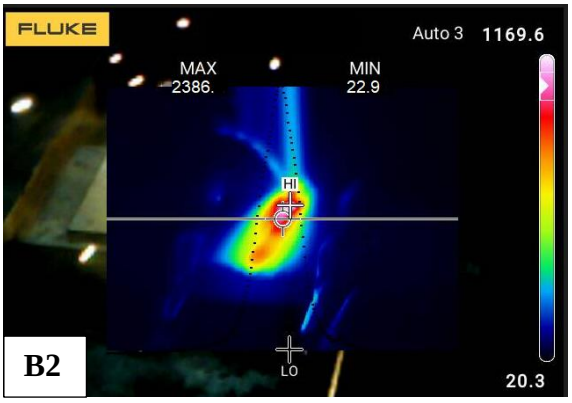

Figure 4.9: Temperature at 90A welded by E316L-16

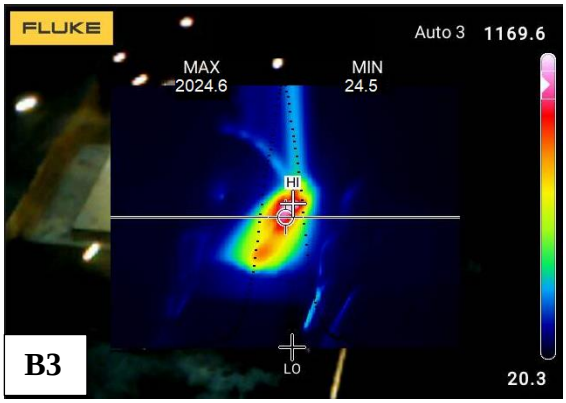

Figure 4.10: Temperature at 100A welded by E316L-16

Figure 4.10 displays a slightly different temperature range, with a minimum of 24.5°C and a maximum of 2024.6°C, and a welding current of 100A. Similar to the previous image, this one also displays a heat concentration with a marked "HI" point indicating the hottest color. The

thermal images use a color gradient to represent temperature variations, with red representing the hottest areas and blue the cooler areas. The central hot spot corresponds to the weld pool, with heat dissipating outward.

4.5 Methodology of Thermal Analysis

The thermal study of the welded zone was conducted using the student edition of ANSYS 2024 R1. All necessary analyses for thermal assessment have been carried out within the transient temperature range.

4.5.1 Geometry Creation

ANSYS design modeler is a versatile and user-friendly tool that plays a crucial role in the simulation workflow, from initial geometry creation to preparing models for analysis. Its comprehensive feature set allows engineers to efficiently develop accurate and detailed models, which are essential for reliable simulation results. For this present study, the entire model geometry was constructed in ANSYS using its design modeler. The investigation utilized dissimilar plates of the same size for both electrodes.

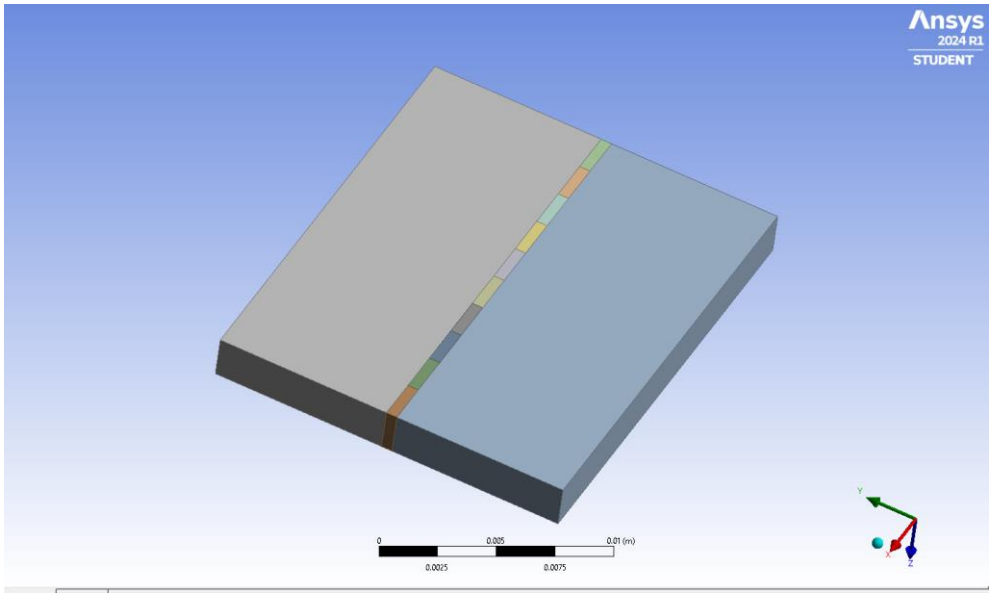

Figure 4.11: Initial geometry of welded specimen

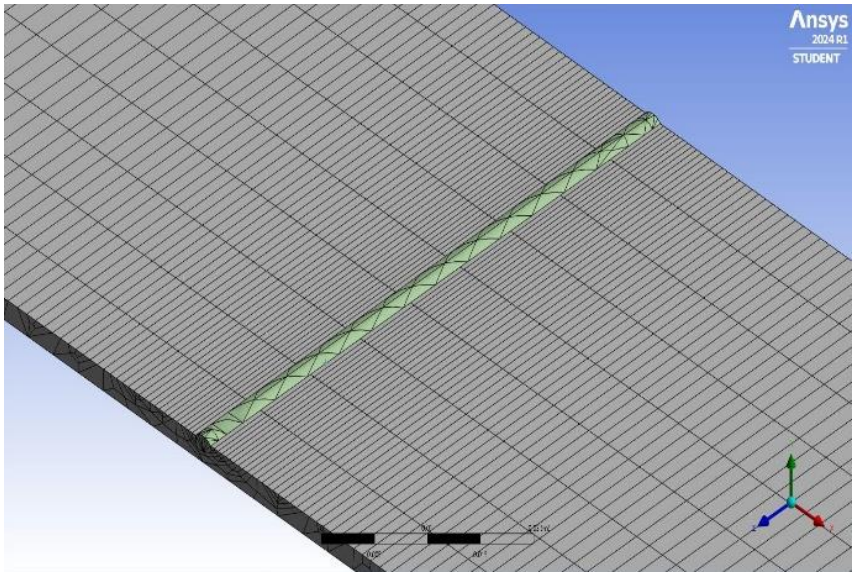

Figure 4.12: Geometric area of welded specimen

The initial setup, illustrated in figure 4.11 featured two plates, each measuring 60 mm by 60 mm by 2 mm, joined using SMAW techniques. A half-circle with a 1 mm diameter was incorporated into the models to indicate the welding area, with the welded zone having a penetration depth of 2 mm. Figure 4.12 shows the geometric area of welded specimen.

4.5.2 Meshing

Meshing in ANSYS involves subdividing a geometry into smaller, finite elements to enable numerical analysis in simulations, a procedure known as finite element meshing. This process is a fundamental component of the finite element analysis (FEA) workflow. Essentially, meshing transforms the geometry into simpler, discrete pieces called elements, which are interconnected at points known as nodes. The elements can vary in type 1D elements are used for line structures like beams, 2D elements for planar structures like shells, and 3D elements for solid structures, which can include tetrahedral, hexahedral, or other shapes. In the current study, two plates, each 60 mm by 60 mm and 2 mm thick, are used, with the welding area depicted as a half-circle with a 1 mm diameter. For meshing, an element size of approximately 1 mm was chosen for the plates, while a finer element size of 0.1 mm was used for the welding area to achieve greater detail. After generating the mesh, its quality was assessed by reviewing mesh statistics and parameters such as aspect ratio, skewness, and element quality to ensure it meets the required accuracy standards. Figure 4.13 displays meshing of the welded specimen and figure 4.14 shows skewness meshing of the welded specimen.

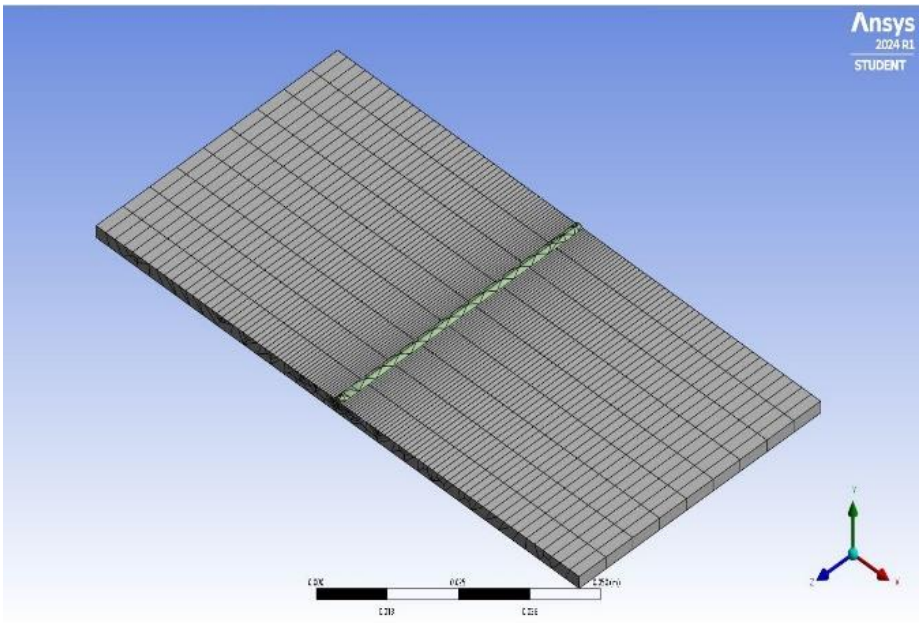

Figure 4.13: Meshing of the welded specimen

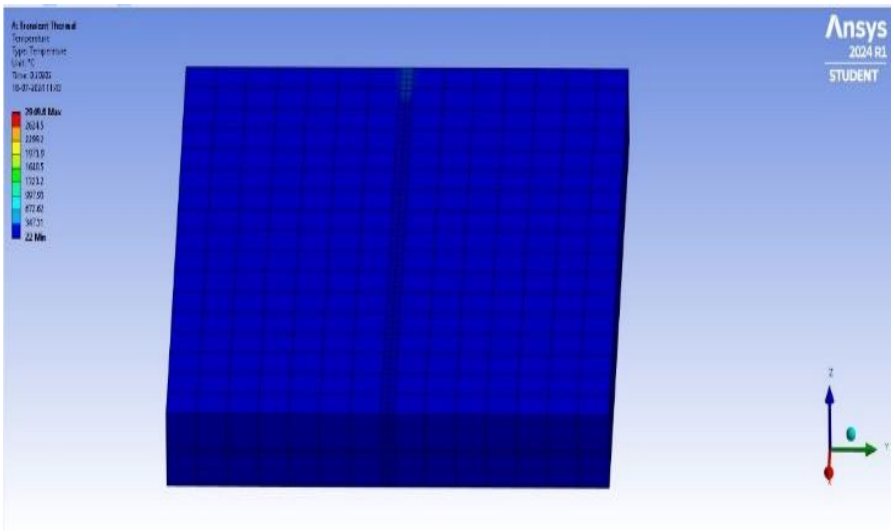

Figure 4.14: Skewness meshing of the welded specimen

4.5.3 Material Assignment and Boundary Conditions

SMAW techniques were employed to weld DSS 2205 and 316L stainless steel materials. The thermal and mechanical properties of these base materials, listed in Table 4.4 [81], were entered into ANSYS engineering data for the analysis of both the plate geometry and the welded region. For the simulation, the plates and the welded region were modeled with the same properties for DSS 2205 and SS316L, capturing the melting and joint formation that occur during welding.

In transient thermal analysis using ANSYS, boundary conditions are crucial for defining how heat is applied, removed, or distributed within the model over time. These conditions include specifying a temperature at points or surfaces, which can be either constant or vary with time, to set initial temperatures or apply specific thermal conditions. The boundary condition for the transient thermal analysis was set at an ambient temperature of 33 °C. A convection heat coefficient, or film coefficient, of 5.0 W/ (m²•°C) was applied to the plate body geometry for steel. The heat flux, determined from experimental measurements of the welding time, was applied to the welded area.

Table 4.4: Thermal properties of base Metal of SS316L & DSS 2205 [81, 83, and 84]

Base Metal	Ultimate Tensile Strength (MPa)	Yield Strength (MPa)	Modulus of Elasticity (GPa)	Vickers Hardness HV	Specific Heat Capacity(J/g-°C)	Thermal Conductivity (W/(m·K)	Density (Kg/m3)
SS316L	515	205	193	155	0.500	14.0-15.9	7817
DSS 2205	655	450	200	293	0.500	15.0	7800

4.5.4 Solution

Two types of electrodes, E316L-16 and ER 2209, were used in the welding process. These electrodes facilitated the welding of SS316L and DSS 2205 materials using the SMAW method. The heat input and heat flux were calculated using Equations 3.3 and 3.4, along with the welding parameters. The results of this analysis are presented in Table 4.5.

Table 4.5: Utilization of electrodes ER 2209 and E316L-16

Specimens	Current (A)	Voltage (V)	Welding speed (mm/min)	Heat input, (kJ/mm)	Heat flux, (W/mm^2)
A1	80	24	189.873	0.606	3.192
A2	90	24	215.827	0.600	2.787
A3	100	24	251.046	0.573	2.282
B1	80	24	172.910	0.666	3.855
B2	90	24	206.185	0.628	3.046
B3	100	24	231.660	0.621	2.687

Observations reveal that for all A specimens, an increase in welding current is linked to a higher welding speed when using electrode ER2209. This suggests reduced heat input, as the electrode remains in contact with the base metal for a shorter period. For example, specimen A1, with an 80A current and a welding speed of 189.873 mm/min, exhibited the highest heat input value (0.606 KJ/mm) among all A samples using electrode ER2209. However, when the welding speed was increased to 215.827 mm/min at 90A, the heat input decreased to 0.600 KJ/mm. As observed in the macrostructure of all A samples, this can reduce the size of the total heat-affected zone (HAZ), potentially minimizing distortion and heat-related issues in the weldment. Additionally, the deposited weld metal cools more rapidly because of the increased welding speed. As evident from the microstructure of sample A, this rapid cooling can affect the microstructure, resulting in a finer grain structure. This finer grain structure enhances the weld's mechanical properties, such as strength and toughness. Additionally, as observed, increasing the welding speed may reduce weld penetration. The macrostructure of all A samples shows some penetration. This is due to the limited weld penetration depth into the joint caused by the shorter duration of the arc's contact with the base metal. Increased welding speeds often lead to longer and narrower weld beads, which can alter the overall appearance of the weld. Similar results were observed when electrode E316L-16 was used in specimen samples B. Increasing both the welding speed and current led to a reduction in heat input. When welded at a speed of 172.910 mm/min and with an 80A current, specimen B1 using electrode 316L-16 exhibited the highest heat input value among all B samples, measuring 0.666 KJ/mm. However, when the welding speed increased to 206.185 mm/min at 90 A, the heat input value decreased to 0.628 KJ/mm, as shown in Table 4.5.

4.5.5 Temperature Distribution

Specimen A1 was analyzed to assess the temperature distribution and pinpoint the maximum and minimum temperatures on the welding plate. Further data regarding welding parameters and equations were gathered and incorporated into ANSYS's transient thermal analysis. Figures 4.15 and 4.16 represents the temperature distribution on specimen A1 and B1, welded with electrode ER2209 and E316L-16 at an 80A current, at various time period. Figure displays the temperature distribution using a color map, with lower temperatures represented by blue or green, transitioning through intermediate colors like yellow or orange, and higher temperatures shown in red, indicating warmer temperatures. Additionally, the figure illustrates that along the

plate, the temperature decreases from the red-colored welded zone to the blue-colored region. A heat flux of 3.192 W/mm² is applied to the welded region of specimen A1.

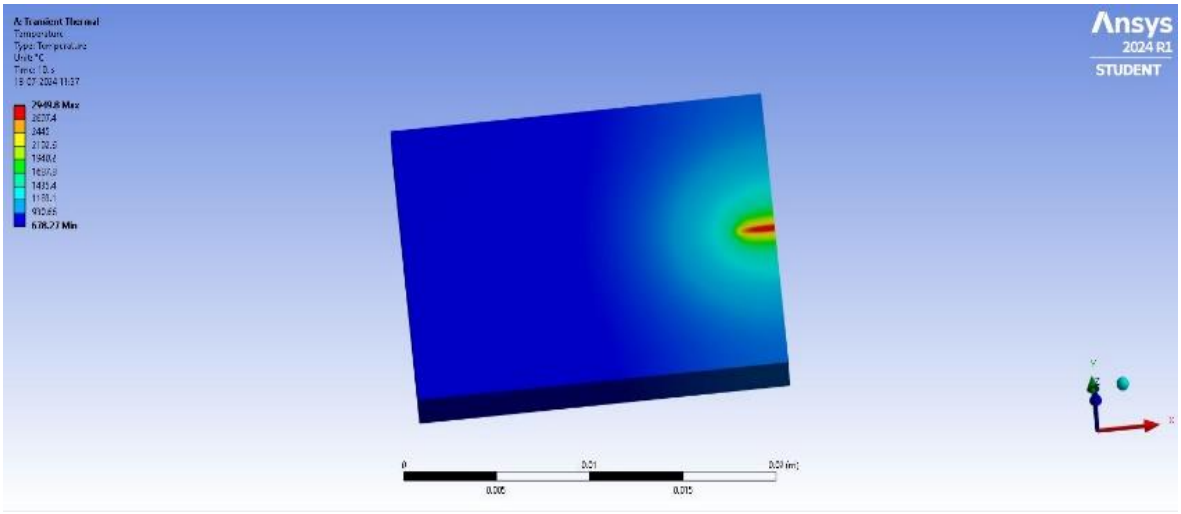

Figure 4.15: Temperature distribution on the specimen (A1) at current 80A

The welding process takes 18.96 seconds to complete. According to the analysis results, the highest temperature in the welding region, indicated by its red color, is 2936.6 °C. However, the plate's blue color indicates that the lowest temperature is 23.3°C. Table 4.6 presents the highest and lowest temperatures in the welded samples, analyzed using electrodes ER2209 and E316L-16 for specimens A1 and the other samples A2, A3, B1, B2, and B3. The welding of sample A1 took 18.96 seconds to complete, and the table indicates that it reached a maximum temperature of 2936.6 °C. In contrast, sample A2 had a lowest recorded temperature of 2280.2 °C and took 16.72 seconds to complete. Similarly, sample B1 reached a maximum temperature of 3056.2 °C and required 20.84 seconds to complete. Sample B3 was finished in 15.58 seconds and had the lowest maximum temperature reported at 2024.6 °C. This indicates that, for both specimens, the temperature decreases as the welding time shortens. A shorter arc length produces less heat, which aligns with the observed correlation in heat input. Longer welding

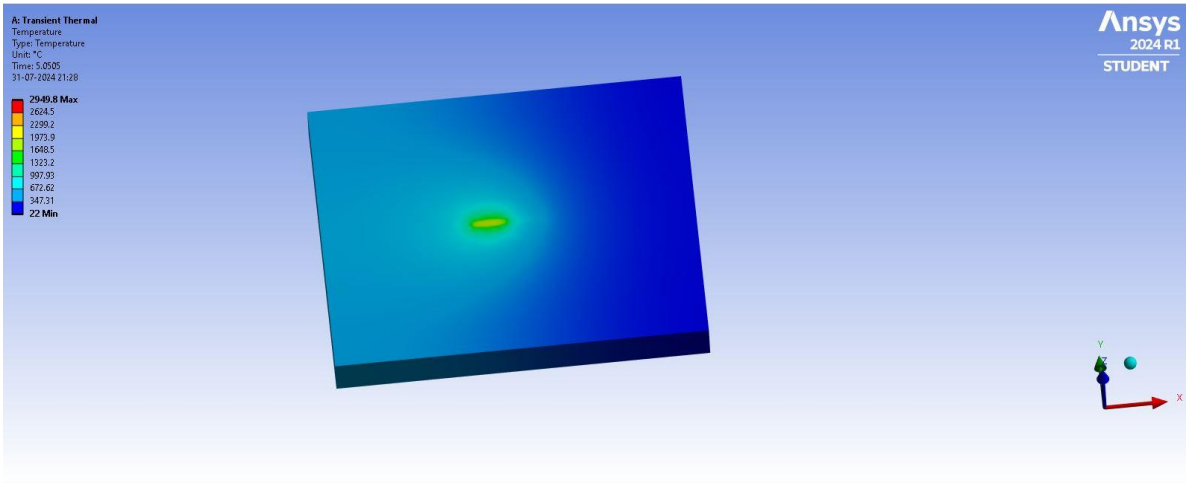

Figure 4.15: Temperature distribution on the specimen (B1) at current 80A

Table 4.6: Maximum and minimum temperature of welded specimens

Specimen	Time (sec)	Maximum temperature (°C)	Minimum temperature (°C)
A1	18.96	2936.6	23.3
A2	16.72	2280.2	23.3
A3	14.34	1906.4	24.3
B1	20.84	3056.2	25.2
B2	17.46	2386.5	22.9
B3	15.58	2024.6	24.5

4.5.6 Heat Flux Analysis

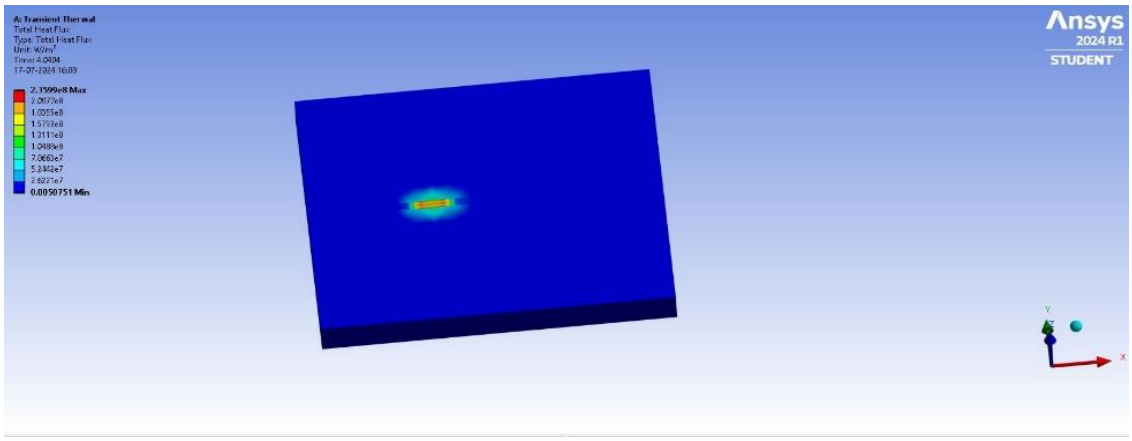

Figure 4.17: Heat flux distribution on the specimen (A1) at current 80A

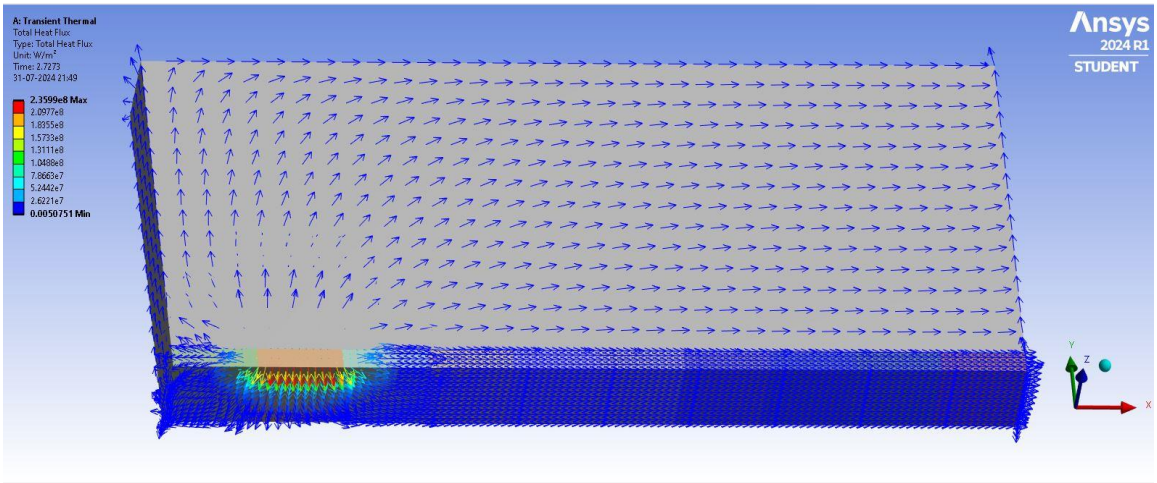

Figure 4.18: Heat flux distribution in the vector form on the specimen (A1) at current 80A

Figure 4.17 displays the heat flux distribution on the specimen (A1) at current 80A and figure 4.18 shows the heat flux distribution in the vector form on the specimen (A1) at current 80A.

The below mention graph represents the relationship between current (Amperes) and heat flux (W/mm²) for two different types of electrodes: ER2209 and ER316L.

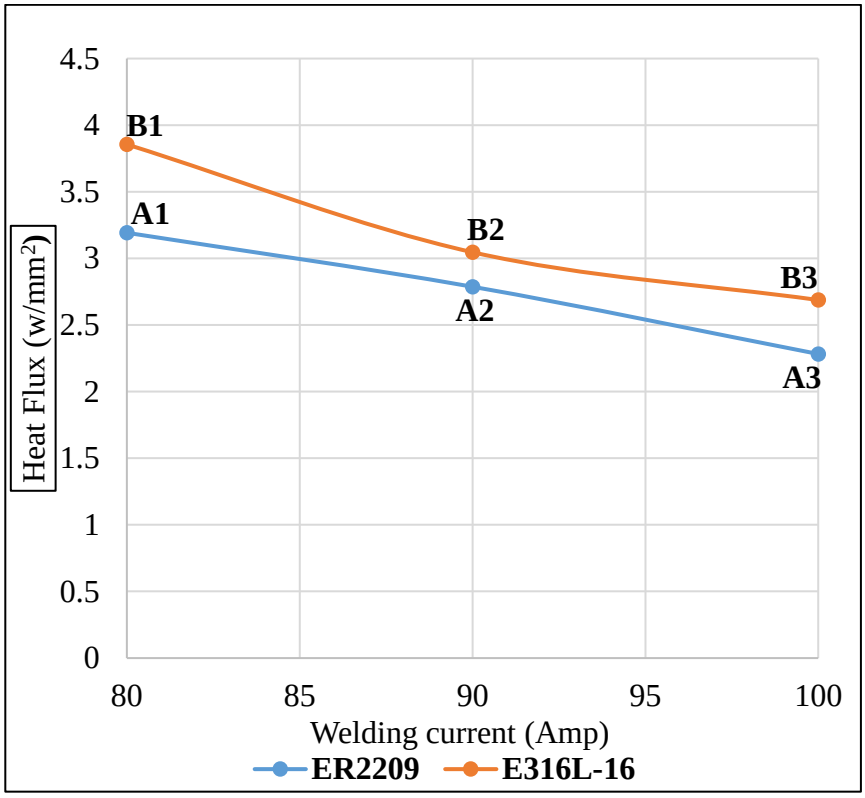

Figure 4.19: Heat flux versus current (A) for two different types of electrode

Graph illustrates the relationship between welding current (Amperes) and heat flux (W/mm²) for two types of electrodes, ER2209 and E316L-16. As the welding current increases from 80A to 100A, both electrodes exhibit a decrease in heat flux. Specifically, the heat flux for ER2209 decreases from 3.1 W/mm² to 2.5 W/mm², while for E316L-16, it decreases from 3.9 W/mm² to 2.8 W/mm². According to the equations 3 and 4 provided, heat input is directly proportional to welding current (I) when voltage (V) and welding speed (S) are held constant, suggesting that heat input should theoretically increase with increasing current. Heat flux, which measures the distribution of heat input over the weld area, decreases as welding speed (S) or the length of the weld bead (L) increases. Therefore, if welding speed (S) increases with welding current, the heat input per unit length decreases, resulting in lower heat flux. Higher welding speeds cause the weld to move faster, reducing the amount of heat deposited in a specific area and leading to lower heat flux. E316L-16 consistently shows higher heat flux than ER2209 at similar currents, indicating it transfers heat more efficiently due to differences in material properties, thermal conductivity, or deposition rates of the electrodes.

4.6 Microstructural Analysis

As shown in figure 4.20 to 4.25, it illustrate the optical microstructures of DSS 2205 and 316L stainless steel weldments at different magnifications, revealing various phases and grain structures. In specimen A, the microstructures of SS316L and DSS 2205 are depicted at 200 µm and 500 µm magnifications. These images distinctly show phases such as martensite, cementite, and pearlite, highlighting different regions within the weldment. Notably, martensite, which is typically hard and brittle, is observed. Additionally, the 500 µm magnification images focus on the weld bead cross-section where SS316L and DSS 2205 have melted and blended during welding, significantly impacting the weld's mechanical properties. In specimen B, also magnified at 500 µm, the microstructure displays fine grain structures. The uniformity and size of these grains offer insights into the thermal history and cooling rates during welding. Martensite is observed, indicating areas of higher hardness and potential brittleness. When comparing specimens A and B, the presence of martensite is a consistent feature in the weldments, affecting toughness and hardness. The fusion zones in both specimens demonstrate successful melting and mixing of the base materials, 316L and DSS 2205. These microstructures are essential for evaluating weld quality, with fine grain structures suggesting effective welding and uniform cooling rates.

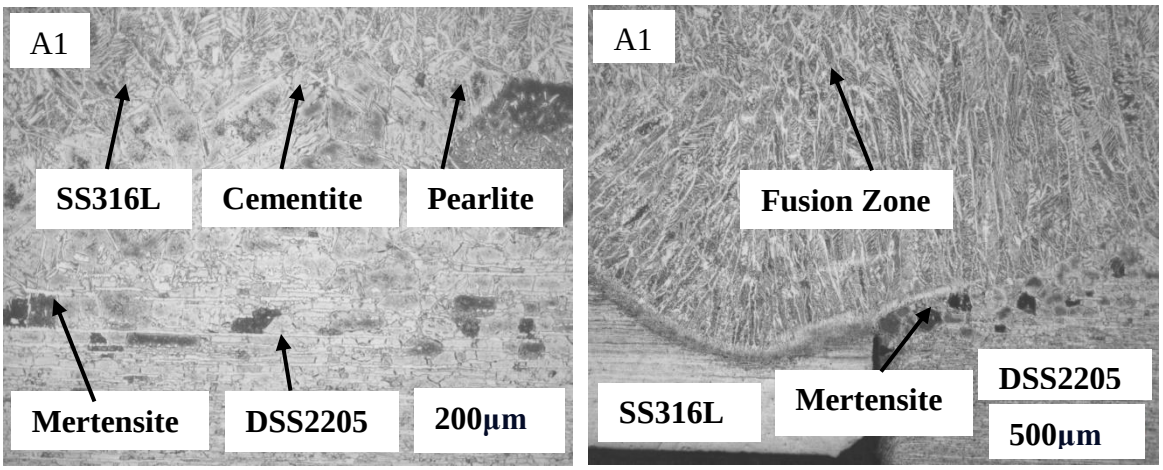

Figure 4.20: Optical microstructure of A1 at 200µm and 500µm

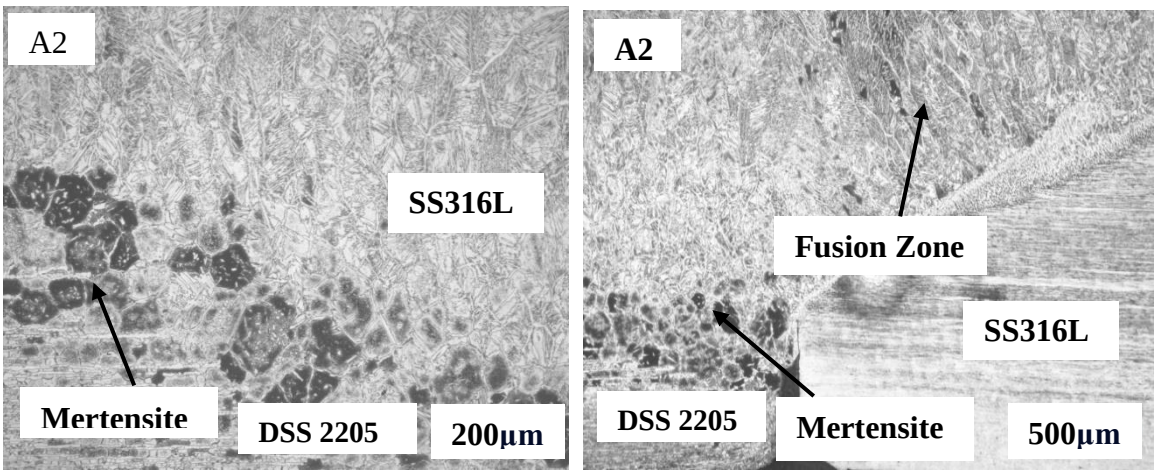

Figure 4.21: Optical microstructure of A2 at 200µm and 500µm

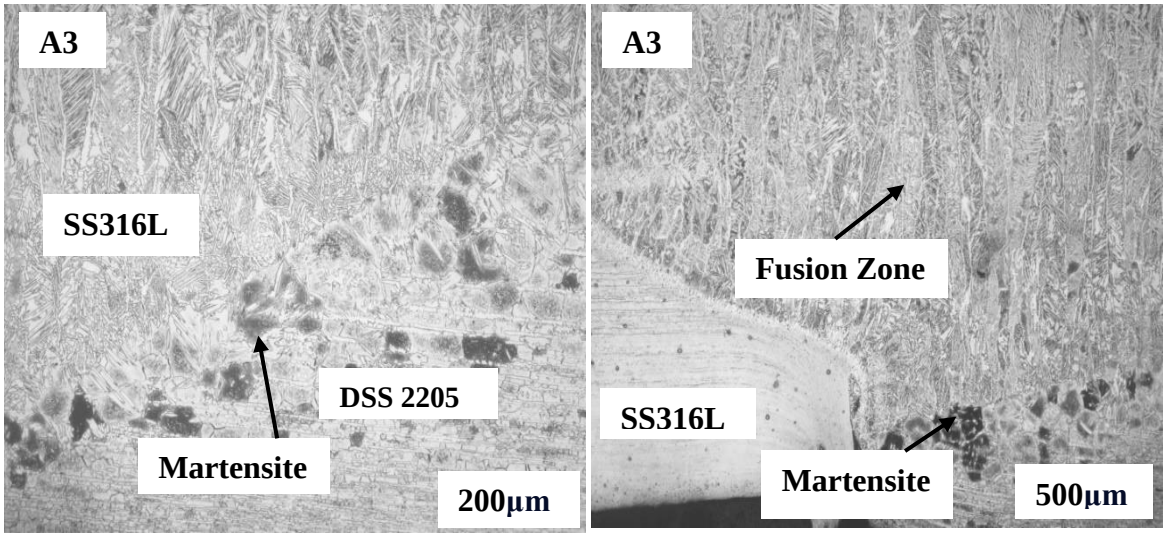

Figure 4.22: Optical microstructure of A3 at 200µm and 500µm

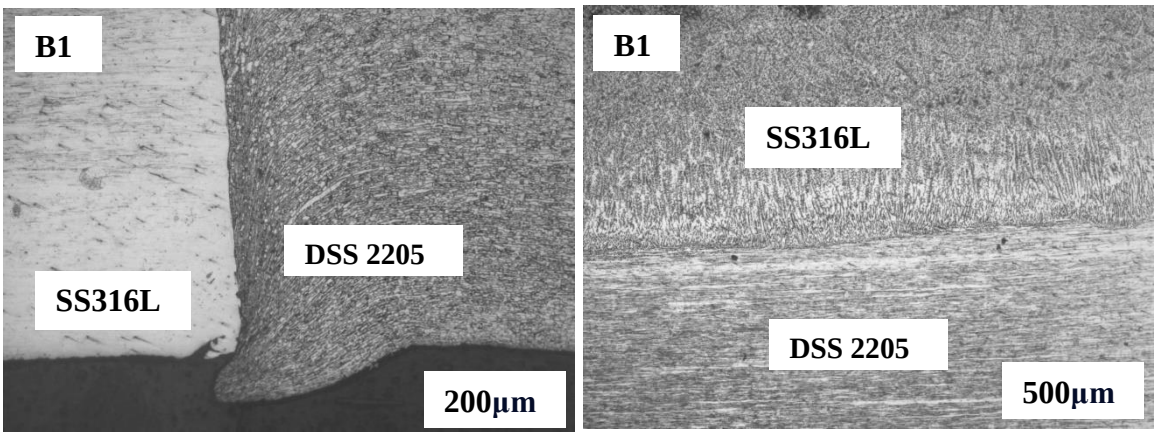

Figure 4.23: Optical microstructure of B1 at 200µm and 500µm

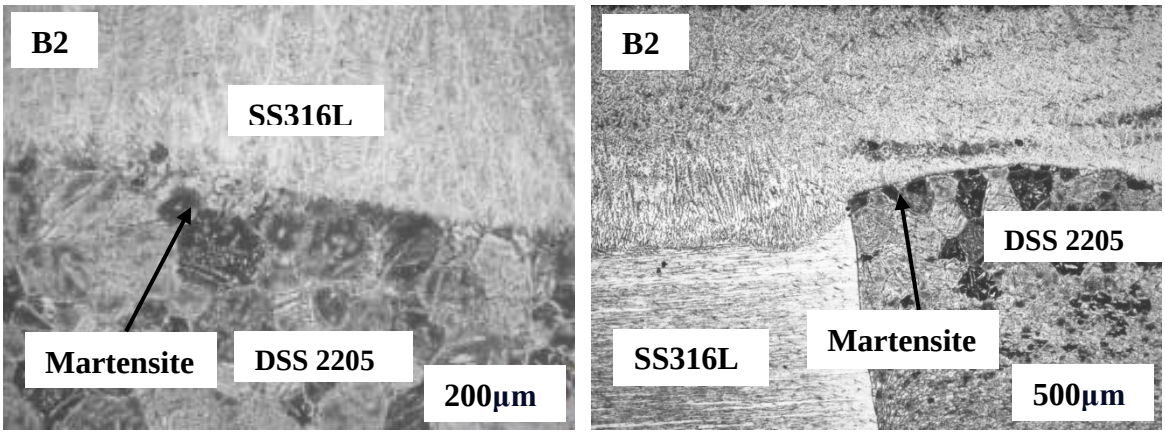

Figure 4.24: Optical microstructure of B2 at 200µm and 500µm

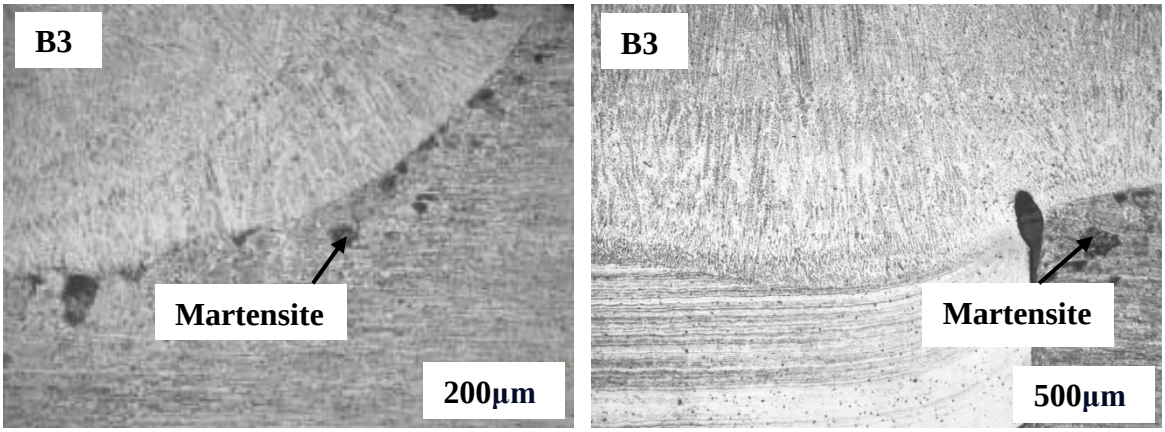

Figure 4.25: Optical microstructure of B3 at 200µm and 500µm

316L Stainless Steel is an austenitic stainless steel primarily made up of austenite (γ-Fe) with a face-centered cubic (FCC) structure. Ferrite is usually minimal in 316L due to its austenitic nature, although it may appear as a light phase if present, usually resulting from specific solidification conditions or heat treatments. Cementite is also minimal in 316L due to its low carbon content and high levels of chromium and nickel, which stabilize the austenite phase. Pearlite, typically formed in carbon steels during cooling, is absent in 316L. Martensite, a hard phase resulting from rapid cooling of austenite, is generally not found in 316L under normal conditions but may appear as a dark phase under extreme conditions or specific heat treatments. In contrast, Duplex 2205 Stainless Steel is a duplex stainless steel that features a microstructure with both ferrite (α-Fe) and austenite (γ-Fe) phases. Ferrite makes up approximately 40-50% of the microstructure and appears as a light or white phase in optical micrographs due to its body-centered cubic (BCC) structure, which enhances the steel's strength and toughness. While cementite is not a major phase under normal conditions, it may form in small amounts during prolonged exposure to high temperatures, appearing as a dark phase. Like 316L, Duplex 2205 typically lacks pearlite, as its formation is characteristic of carbon steels. Martensite is not a primary phase in Duplex 2205 but may form in small amounts during specific heat treatments or welding processes, potentially appearing as a dark, hard phase that can influence local mechanical properties.

Overall, optical microscopy of these microstructures provides valuable insights into the phases formed during welding, the quality of the welds, and the potential mechanical properties of the joints. The presence of ferrite, cementite, and pearlite further aids in understanding the complex interactions and transformations occurring during welding. 316L stainless steel predominantly

consists of austenite, with minimal ferrite, cementite, pearlite, or martensite. Duplex 2205 stainless steel features a balanced combination of ferrite and austenite, with possible minor phases of cementite and martensite depending on processing conditions, while pearlite is generally absent. Understanding these phases and their formation is crucial for optimizing the mechanical properties and performance of these stainless steels in various applications.

CHAPTER 5

CONCLUSION AND FUTURE SCOPE

5.1 Conclusion

In the current research work, the shielded metal arc welding is employed to join two dissimilar materials, duplex stainless steel 2205 and austenitic stainless steel 316L, by using varying currents (80 A to 100 A) and two different types of electrodes (ER2209 and E316L-16). The study examined the effects of these process parameters on mechanical properties, weld deposition, fusion zone, microstructure, heat flux, and temperature distribution in the weldments, and their correlation with the microstructure. The finding can be withdrawn from the present study as given below:

1. It is observed from the experimentation that weld deposition initially increases with an increase of welding current up to 90 A, and thereafter, it declines as welding current increases by using both electrodes ER 2209 and ER 316L. ER 2209 electrode shows higher weld deposition rate as compared to ER 316 L electrode.

2. Weld seam width increases with an increase of welding current up to 90 A, followed by declines in weld seam width as welding current further increases. This behaviour is shown by using both electrode ER 2209 and ER 316L.

3. ER 2209 electrode welded sample exhibits higher fusion zone width relative to ER 316L welded material, due to differences in their metallurgical and chemical properties, affecting their melting and solidification behaviours during the welding process.

4. Ultimate tensile strength of ER 2209 welded sample initially increases from 485 N/mm² to 626 N/mm² as the welding current increases from 80 A to 90 A. However, with a further increase in current from 90 A to 100 A, the ultimate tensile strength decreases from 626 N/mm² to 566 N/mm². The ultimate tensile strength of ER 316 L welded materials initially increases from 416 N/mm² to 558 N/mm² as the current increases from 80 A to 90 A, but then decreases from 558 N/mm² to 509 N/mm² as the current rises from 90 A to 100 A. This also signifies that ER 2209 welded sample gives better strength compared to ER 316L electrode. The yield strength also shows the same behaviour.

5. Transient thermal analysis based on finite element method is performed using ANSYS software, and temperate of fusion zone is calculated, and the same is validated with experimental results, as captured by the infrared thermal image.

6. The thermal analysis of duplex stainless steel 2205 and austenitic stainless steel 316L reveals that as the welding current increases, the time required to complete the weld decreases in all samples. Additionally, the temperature of both electrode samples decreases as the welding time decreases, as indicated by the simulation results. The temperature distribution of the samples along the plate was also observed in different regions.

7. The optimal combination of welding parameters resulted in weldments with a balanced microstructure, minimal defects, and favorable mechanical properties.

5.2 Future Scope of the Research

Although DSS 2205 and 316L weldment, characterization, and property evaluation have been made in the current study utilizing current and electrodes, many more studies need to be conducted, which was outside the purview of the investigation. These studies can be summed up as follows:

1. Strength and corrosion analysis of the weldment required for use in ship construction.

2. In subsequent research, more marine-grade materials and welding techniques - particularly high-energy beam welding - will be included in addition to the examination of other factors, such as corrosion tests.

3. A comparison of the weldment parametric study and cost across several processing routes.

4. To precisely measure the temperature along the welded area and assess its effect on the plate, future tests will make use of sophisticated temperature measuring instruments including K-type thermocouples, Fluke devices, and comparable tools.

5. In addition, the APDL (Ansys Parametric Design Language), which enables complex engineering simulations based on the Finite Element Method (FEM), will be used to do a more thorough thermal analysis.

CHAPTER 6

REFERENCES

1. Turan, Eda & Koçal, Tarık & Ünlügençoglu, K.. (2011). Welding Technologies In Shipbuilding Industry.
2. Kumar, N. Kumar, A. Gupta, A. Gaikwad, A.D. Khatirkar, R.K. (2018). Gas Tungsten ArcWelding of 316 L Austenitic Stainless Steel with UNS S32205 Duplex Stainless Steel Trans. Indian Inst. Met., 71, 361–372.
3. Rahmani, M. Eghlimi, A. Shamanian, M. (2014). Evaluation of microstructure and mechanical properties in dissimilar austenitic/super duplex stainless steel joint. J. Mater Eng. Perform, 23, 3745–3753.
4. Gunn, R.N. (1997). Duplex Stainless Steels: Microstructure, Properties and Applications Cambridge: Abington Publishing,Woodhead Publishing Ltd.
5. Labanowski. (1997). Duplex stainless steels—New material for chemical industry. Appar. Chem. Eng., 36, 3–10.
6. Lippold, J.C. Kotecki, D.J. (2005). Welding Metallurgy and Weldability of Stainless Steels Hoboken, NJ, USA: Wiley Publications.
7. Kumar. A. Pandey C. (2022). Autogenous laser-welded dissimilar joint of ferritic/martensitic P92 steel and Inconel 617 alloy: Mechanism,microstructure, and mechanical properties Arch. Civ. Mech., 22-39.
8. Geng.S, Sun, J. Guo, L. Wang, H. (2015). Evolution of microstructure and corrosion behavior in 2205 duplex stainless steel GTA-welding joint. J. Manuf. Process, 19, 32–37.
9. Luo J, Liu DJ, Zhao GJ, Wang XJ, Ran HQ. (2011). Relationship between microstructure of fusion zone and mechanical properties of 2205 duplex stainless steel joint in double-sided submerged arc welding. Rare Metal Materials and Engineering, 40(3), 69–74.
10. Antony PJ, Singh Raman RK, Kumar P, Raman R. (2008). Corrosion of 2205 duplex stainless steel weldment in chloride medium containing sulfate-reducing bacteria Metallurgical and Materials Transactions A, 39(26), 89–97.

11. Sathiya P, Aravindan S, Soundararajan R, Noorul Haq A. (2009). Effect of shielding gases on mechanical and metallurgical properties of duplex stainless-steel welds. Journal of Materials Science, 44(1), 14–21.

12. Ureˇna A, Otero E, Utrilla MV, Munez CJ. (2007). Weldability of a 2205 duplex stainless steel using plasma arc welding. Journal of Materials Processing Technology, 182(6), 24-34.

13. Journal of Materials Processing Technology. (n.d.). Effect of Filler Materials on Mechanical Properties of Shielded Metal Arc Welded AISI 316L Austenitic Stainless Steel Joints.

14. J. Charles. (1991). Conf proc Duplex Stainless Steels '91. Beaune: Les editions de physique.

15. R. N. Gunn. (1997). Duplex Stainless Steels: Microstructure, properties and applications Woodhead Publishing.

16. A. Wensley, C. Reid. (1992). Stainless Steel Europe. 32-38.

17. Stainless steel in concrete. State of the art report. (1996). European Federation of Corrosion/The Institute of Materials, 12(3).

18. J. Charles. (1991). Conf proc Duplex Stainless Steels '91. Beaune: Les editions de physique.

19. Baghel PK. Effect of SMAW process parameters on similar and dissimilar metal welds: An overview. Heliyon. 2022 Dec 9;8(12):e12161. doi: 10.1016/j.heliyon.2022.e12161.PMID: 36578398; PMCID: PMC9791349.

20. A. S. Abdel-Wanees, T. S. Mahmoudand I. M. Ibrahim. (n.d.). Effect of Electrode Material on Microstructural and Mechanical Characteristics of AISI 304 Stainless Steels Plates Joined Using Shielded Metal Arc Welding.

21. Panwala, M. & Channiwala, S. & Srinivasan, K. (2009). Numerical Simulation of Transient Temperature in SMAW. American Society of Mechanical Engineers.

22. E.C. Bain, W.E. Griffiths. (1927). Trans AIME.

23. P.J. Antony, R.K. Singh Raman, P. Kumar, and R. Raman, Corrosion of 2205 Duplex Stainless Steel Weldment in Chloride Medium Containing Sulfate-Reducing Bacteria, Metall. Mater. Trans. A, 2008, 39(11),p 2689–2697 (in English)

24. I.C. Kuo, C.P. Chou, C.F. Tseng, and I.K. Lee. (2009). Submerged Arc Stainless Steel Strip Cladding-Effect of Post-Weld Heat Treatment on Thermal Fatigue Resistance. J. Mater. Eng. Perform, 18(2), 54–161.

25. A. Bhattacharya and P.M. Singh. (2007). Stress Corrosion Cracking of Welded 2205 Duplex Stainless Steel in Sulfide-Containing Caustic Solution. J. Fail. Anal. Prev, 7(5), 371–377.

26. Muthupandi V, Bala Srinivasan P, Seshadri SK, Sundaresan S. (2003). Effect of weld metal chemistry and heat input on the structure and properties of duplexstainless steel welds Mater Sci Eng, 9–16.

27. Yang Y, Yan B, Li J, Wang J. (2011). The effect of large heat input on the microstructure and corrosion behaviour of simulated heat affected zone in 2205 duplexstainless steel Corros Sci, 53(37), 56–63.

28. Kang DH, Lee HW. (2013). Study of the correlation between pitting corrosion and the component ratio of the dual phase in duplex stainless steel welds. Corrosion Sci, 74, 396–407.

29. J. LABANOWSKI, K. KRZYSZTOFOWICZ and K. SAMSON. (n.d.). Investigations into the tendency to stress corrosion of joints welded in austenitic and duplex steels. Department of Materials Engineering, Gdansk Polytechnic.

30. Shukla, Amarish & Gond, Dinesh & Puri, Doron. (2016). Effect of Cold Working on Hot Corrosion Behavior of 9 Cr–1 Mo Ferritic Steel in 75 wt% Na2SO4 + 25 wt% K2SO4 Molten Salt Environment at 900 °C. Transactions of the Indian Institute of Me.

31. https://www.stripdrains.com.au/blog/316-stainless%20steel/

32. Fajobi, M. A., Loto, T. R., & Oluwole, O. (2021). Austenitic 316L Stainless Steel Corrosion and Organic Inhibitor: A Review. Key Engineering Materials, 886, 126–132.

33. Ghosh, N.; Pal, P.K.; Nandi, G. (2017). GMAW dissimilar welding of AISI 409 ferritic stainless steel to AISI 316 L austenitic stainless steel by using AISI 308 filler wire. Eng Sci.Technol. Int. J., 20, 1334–1341.

34. Maurice Stewart. (2021) Science direct. Retrieved 2024, from https://www.sciencedirect.com/topics/engineering/shielded-metal-arc-welding

35. Ramakant Sharma. (2020) cruxweld. Retrieved from https://www.cruxweld.com/blog/submerged-arc-welding/

36. Bruce Morrett. (2002). The Welder Retrieved from https://www.thefabricator.com/thewelder/article/arcwelding/helpful-tips-for-how-timprove-your-gmaw-weld

37. Maurice Stewart. (2021). Science direct. Retrieved from https://www.sciencedirect.com/topics/engineering/gas-tungsten-arc welding#:~:text=Gas%20tungsten%20arc%20welding%20

38. GIHAD IBRAHIM. (n.d.). mechasource. Retrieved from https://mechasource.blogspot.com/2018/06/oxyacetylene-welding-introduction-and.html

39. Binoy K. Biswas, Asish Bandyopadhyay and Pradip K. Pal. (n.d.). A study on quality of weld in flux cored arc welding process. Mechanical Engineering Department, Jadavpur University.

40. https://www.sciencedirect.com/topics/engineering/flux-cored-arc-welding

41. MaidulSakil. (2023). Medium. Retrieved from https://medium.com/@MaidulSakil/what is- flux-core-welding-advantages-disadvantages-bedca16002e2

42. C.A.Walsh. (2002) LASER WELDING - Literature Review. Materials Science and Metallurgy.

43. Morteza Tayebi, Hedayat Mohammad Soltani and Ali Rajaee. (2021) Laser Welding Engineering Principles - Welding and Residual Stresses.

44. Soy, Ugur & Iyibilgin, Osman & Findik, Fehim & Oz, Cemil & Kiyan, Yasar. (2011) Determination of welding parameters for shielded metal arc welding. Scientific Research and Essays.

45. Durgutlu A. (1997) The effect of welding speed on the microstructure and penetration in arc welding. Turkey.

46. Anik S. (1991). Handbook of welding Technique. Istanbul: Gedik welding publications.

47. Yasar Y, Soy U, Aslanlar S, Oz C. (2010) TIG welding method with plate 1070 series aluminum alloys of combining the mechanical properties of the effect of current resources. Turkey: Proceedings of the 13th International Materials Symposium.

48. Black JT, Kohser RA. (2008) Materials & processes in manufacturing. New Jersey: Wiley Interscience.

49. Oguz B. (1993) Handbook of arc welding. Istanbul: Oerlikon Publications.

50. Soy U. (2019) Welding Current Types DCEN, DCEP, AC. Retrieved from https://amarineblog.com/2019/09/03/welding-current-types-dcen dcepac/#:~:text=There%20are%20three%20different%20types

51. JianLuo, YiYuan, Xiaoming Wang, and Zongxiang Yao. (n.d.) Double-Sided Single-Pass Submerged Arc Welding for 2205 Duplex Stainless Steel. 2009.

52. RaffiMohammed, Madhusudhan Reddy G, Srinivasa Rao K. (2015) Effect of Welding Process on Microstructure, Mechanical and Pitting Corrosion Behaviour of 2205 Duplex Stainless Steel Welds.

53. R. Selva Bharathi, N. Siva Shanmugam, R. Murali Kannan and S. Arungalai Vendan. (n.d.). Studies on the Parametric Effects of Plasma Arc Welding of 2205 Duplex Stainless Steel.

54. N.A. McPherson, Y. Li & T.N. Baker. (n.d.) Microstructure and properties of as welded duplex stainless steel.

55. Xiaodong Hu, Lu Qin, Huanqing Wang, Lu Zhang and Xuefang Xie. (n.d.) Microstructure Formation and Its Effect on Mechanical Properties for Duplex Stainless Steel 2205 Plasma ArcWelded Joint.

56. Jian Luoa, Yaling Donga, Longfei Li, Xiaoming Wanga. (n.d.). Microstructure of 2205 duplex stainless steel joint in submerged arc welding by post weld heat treatment.

57. N.A.Mcpherson, K. Chi, T.N. Baker. (n.d.) Submerged arc welding of stainless steel and the challenge from the laser welding process.

58. Aswin S. Kumar, Sumit K. Sharma, and Amarish Kumar Shukla. (n.d.). Microstructural, Mechanical, and Thermal Analysis of SS316L Weldment for Marine Engineering Application.

59. Santina Topolska, Aleksander Gwiazda. (n.d.) Simulation of Properties of Dissimilar Welded Joints of Duplex 2205 and Austenitic 316L Steels.

60. J. Labanowski, K. Krzysztofowicz & K. Samson. (n.d.) Investigations into the tendency to stress corrosion of joints welded in austenitic and duplex steels.

61. Jagesvar Verma, Ravindra Vasantrao Taiwade, Rajesh Kisni Khatirkar and Anil. (n.d.) A Comparative Study on the Effect of Electrode on Microstructure and Mechanical Properties of Dissimilar Welds of 2205 Austeno-Ferritic and 316L Austenitic Stainless Steel.

62. Shaogang Wang, Qihui Ma, Yan Li, Characterization of microstructure, mechanical properties and corrosion resistance ofdissimilar welded joint between 2205 duplex stainless steel and 16MnR

63. Dhananjay Parashar Tumu, P Subramani, K Gokul Kumar, M Manikandan, C G Mohan, N Arivazhagan, Deva N.Rajan. (n.d.). Investigation on microstructure and tensile properties of dissimilar weld joints between AISI 316l and duplex 2205 stainless steel.

64. A. Moteshakker, I. Danaee ,S. Moeinifar and A. Ashrafi. (n.d.). Hardness and tensile properties of dissimilar welds joints between SAF 2205 and AISI 316L.

65. A. Vinoth Jebaraj,T. Sampath Kumar,M. Manikandan. (n.d.). Investigation of Structure Property Relationship of the Dissimilar Weld Between Austenitic Stainless Steel 316L and Duplex Stainless Steel 2205.

66. Aboulfazl Moteshakker, Iman Danaee. (n.d.). Microstructure and Corrosion Resistance of Dissimilar Weld-joints between Duplex Stainless Steel 2205 and Austenitic Stainless Steel 316L.

67. Jagesvar Verma, Ravindra Vasantrao Taiwade, Rajesh Kisni Khatirkar Sanjay G. Sapate,Ashvin D. Gaikwad. (n.d.). Microstructure, Mechanical and Intergranular Corrosion Behavior of Dissimilar DSS 2205 and ASS 316L Shielded Metal Arc Welds.

68. S Topolska. (n.d.). Hardness analysis of welded joints of austenitic and duplex stainless steels.

69. S Topolska. (n.d.). Metallographic investigations of dissimilar welded joints of duplex 2205 and austenitic 316L steels.

70. Topolska and J Łabanowski. (n.d.). Mechanical characteristics of welded joints between different stainless steels grades.

71. The Microstructure and Pitting Resistance of Weld Joints of 2205 Duplex Stainless Steel.

72. A.Balaram Naik, A.Chennakesava Reddy. (n.d.). An Experimental Investigation of Shielded Metal Arc Welding processes on Duplex Stainless Steel to control and correction of distortion in Weldments.

73. Sepe R, Giannella V, Greco A, De Luca A. (2021). FEM Simulation and Experimental Tests on the SMAW Welding of a Dissimilar T-Joint. Metals, 11(7).

74. Hitesh Arora Rupinder Singh,and Gurinder Singh Brar. (n.d.). Thermal and structural modelling of arc welding processes: A literature review.

75. Kamel Touileb, Abdeljlil Chihaoui Hedhibi Rachid Djoudjou, Abousoufiane Ouis, Abdallah Bensalama , Albaijan Ibrahim , Hany S. Abdo, and Mohamed M. Z. Ahmed. (n.d.). Mechanical, Microstructure, and Corrosion Characterization of Dissimilar Austenitic 316L and Duplex 2205 Stainless-Steel ATIGWelded Joints.

76. Fang Ge, Xin Huang, Yi Zhang, Yanfang Song, Xinjing Meng, Honghua Ge, Yuzeng Zhao. (2021). Corrosion Behavior of 2205 DSS Base Metal and ER 2209 Weld Metal in a Deposited Ash/Water Suspension. International Journal of Electrochemical, 16(7).

77. weldguru.com

78. L.O. Osoba, W.A. Ayoola, Q.A. Adegbuji and O.A. Ajibade . (2021). Influence of Heat Inputs on Weld Profiles and Mechanical Properties of Carbon and Stainless Steel. Niger. J. Technol. Dev, 18(2), 135–143.

79. S. Miftin, H. Mohammed and A. Nassar. (2020) Measurement and Prediction of Residual Stresses in Low Carbon Steel Pipe Welded Shielded Metal Arc Welding. Basrah J. Eng. Sci, 20(2).

80. L.O. Osoba, W.A. Ayoola, Q.A. Adegbuji and O.A Ajibade, Influence of Heat Inputs on Weld Profiles and Mechanical Properties of Carbon and Stainless Steel, Niger. J.Technol. Dev., 2021, 18(2), p 135–143.

81. I. AghaAli, M. Farzam, M.A. Golozar and I. Danaee. (2014) The Effect of Repeated Repair Welding on Mechanical and Corrosion Properties of Stainless Steel 316L. Mater. Des, 54, 331–341.

82. V. Gohel, J. Makwana and R. Ranjan. (2016). Thermo-Mechanical Analysis in TIG Welding of SS 304. Int. J. Eng. Dev. Res, 4(2), 1704–1710.

83. ASM aero space specification metals. (n.d.). Retrieved from https://asm.matweb.com/search/SpecificMaterial.asp?bassnum=MQ316Q

84. Atlas Specility Metals. (n.d.). Retrieved from https://www.atlassteels.com.au/documents/Atlas2205.pdf

85. ERHUNMWUN, I. (2017). Review on Finite Element Method.

86. Muhammad A. (2020). Finite Element Analysis of a connecting rod in ANSYS

87. I A Magomedov, Z. S. (2020). Comparative study of finite element analysis software.

88. Ismail, M. W. (2016). Thermal analysis on a weld joint of aluminium alloy in gas metal arc welding

89. Rishi PAMNANI, M. V. (2016). Numerical simulation and experimental validation of arc welding of dmr-249a steel.

90. M Sohel M Panwala, S. A. (2009). Numerical Simulation of Transient Temperature in Smaw

91. Mr.Vodnala, V. P. (2019). Design And Transient Thermal Analysis Of Few Welding Using Conical Tool.

92. SYUKRI, M. S. (2015). Thermal Simulation of Different Welding Speed and Metal Thickness for Butt-Joint welding with ANSYS.

93. AghaAli, M. Farzam, M.A. Golozar and I. Danaee, The Effect of Repeated Repair Welding onMechanical and Corrosion Properties of Stainless Steel 316L, Mater. Des., 2014, 54, p 331–341. https://doi.org/10.1016/j.matdes.2013.08.052.

94 . Saxena, A. Kumaraswamy, G. Madhusudhan Reddy and V. Madhu, Influence of Welding Consumables on Tensile and Impact Properties of Multi-Pass SMAW Armox 500T Steel Joints Vis-a-Vis Base Metal,Def. Technol., 2018, 14(3), p 188–195.

95. Y.Kchaou, N. Haddar, G. He´naff, V. Pelosin and K. Elleuch, Microstructural, Compositional and Mechanical Investigation of Shielded Metal Arc Welding (SMAW) Welded Superaustenitic UNSN08028 (Alloy 28) Stainless Steel, Mater. Des. 2014, 63, p278 285 Https://doi.org/10.1016/j.matdes.2014.06.014.